A Unified Electro- and Photocatalytic CO₂ to CO Reduction Mechanism with Aminopyridine Cobalt Complexes

Sergio Fernández,[a,‡] Federico Franco,[a,‡] Carla Casadevall,[a] Vlad Martin-Diaconescu,[a] Josep M. Luis,[b,*] Julio Lloret-Fillol[a,c,*]

[a] Institute of Chemical Research of Catalonia (ICIQ), The Barcelona Institute of Science and Technology, Avinguda Països Catalans 16, 43007 Tarragona, Spain.

[b] Institut de Química Computacional i Catàlisi (IQCC) and Departament de Química, Universitat de Girona, Campus Montilivi, Girona, E-17003, Catalonia, Spain.

[c] Catalan Institution for Research and Advanced Studies (ICREA), Passeig Lluïs Companys, 23, 08010, Barcelona (Spain).

Supporting Information Placeholder

ABSTRACT: Mechanistic understanding of electro- and photocatalytic CO₂ reduction is crucial to develop strategies to overcome catalytic bottlenecks. In this regard, herein it is presented for a new CO₂-to-CO reduction cobalt aminopyridine catalyst, a detailed experimental and theoretical mechanistic study toward the identification of bottlenecks and potential strategies to alleviate them. The combination of electrochemistry and *in-situ* spectroelectrochemistry together with spectroscopic techniques led us to identify elusive key electrocatalytic intermediates derived from complex [L^{N4}Co(OTf)₂] (**1**) (L^{N4}=1-[2-pyridylmethyl]-4,7-dimethyl-1,4,7-triazacyclononane) such as a highly reactive cobalt (I) (**1$^{(I)}$**) and cobalt (I) carbonyl (**1$^{(I)}$-CO**) species. The combination of spectroelectrochemical studies under CO₂, ^{13}CO₂ and CO with DFT disclosed that **1$^{(I)}$** reacts with CO₂ to form the pivotal **1$^{(I)}$-CO** intermediate at the **1$^{(II/I)}$** redox potential. However, at this reduction potential, the formation of **1$^{(I)}$-CO** restricts the electrocatalysis due to the endergonicity of the CO release step. In agreement with the experimentally observed CO₂-to-CO electrocatalysis at the Co$^{I/0}$ redox potential, computational studies suggested that the electrocatalytic cycle involves striking metal carbonyls. In contrast, under photochemical conditions, the catalysis smoothly proceeds at the **1$^{(II/I)}$** redox potential. Under the latter conditions, it is proposed that the electron transfer to form **1$^{(I)}$-CO** from **1$^{(II)}$-CO** is under diffusion control. Then, the CO release from **1$^{(II)}$-CO** is kinetically favored, facilitating the catalysis. Finally, we have found that visible-light irradiation has a positive impact under electrocatalytic conditions. We envision that light-irradiation can serve as an effective strategy to circumvent the CO poisoning and improve the performance of CO₂ reduction molecular catalysts.

INTRODUCTION

CO₂ reduction is one of the most promising approaches for sustainable production of renewable fuels and chemicals.[1] The design of efficient catalysts for CO₂ reduction entails a fundamental understanding of the parameters that control the catalytic activity and selectivity.[2] However, to obtain insights into the CO₂ reduction mechanism is highly challenging and the mechanism still remains poorly understood.[3] In this regard, coordination complexes serve as platforms to implement different strategies to interrogate the operative mechanisms. Among the differen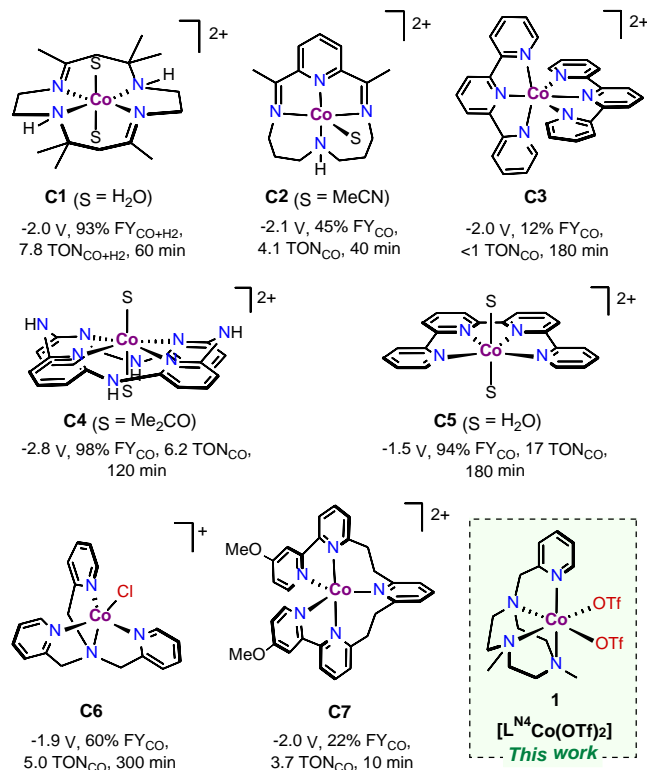t families of active catalysts for CO₂ reduction, cobalt complexes containing polypyridyl or aminopyridyl ligands are easily tunable and therefore of interest for intermediate characterization and mechanistic studies. These cobalt complexes, in combination with specific photosensitizers (*e.g.* Ru[4,5] or Ir[6]) show high activity and selectivity for the light-driven CO₂-to-CO reduction.[7] However, except for some specific examples,[6a,b,8] their electrocatalytic performance is still limited by their low stability and selectivity, resulting in low turnover numbers and faradaic yields (FY) for CO formation (Chart 1, Table S1).[8b,9] Despite many efforts, further understanding of the reaction mechanism is still required to identify the bottlenecks of the electrocatalytic reaction and to explain the differences in performance between the photo- and electrocatalytic conditions.[7b,8a,10,11]
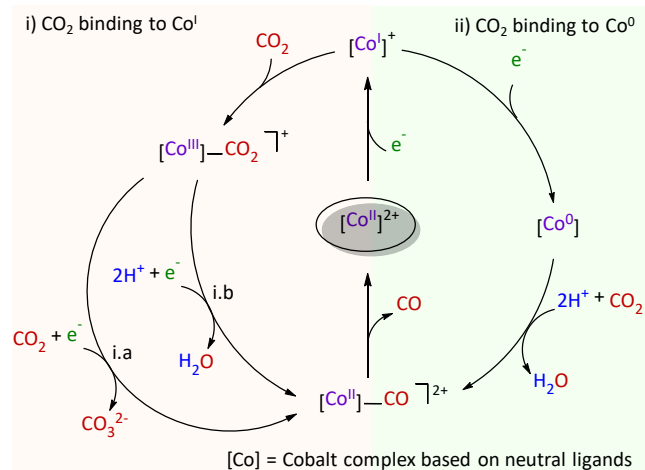
Scheme 1. Summary of the hypothesized mechanisms for electrocatalytic CO₂ reduction to CO by molecular cobalt complexes bearing neutral nitrogen chelating ligands. A formal oxidation state is given for the different Co species.

The most commonly accepted hypotheses for CO₂-to-CO mechanism catalyzed by Co complexes based on nitrogen donor ligands are summarized in Scheme 1. For several reported Co^{II} complexes containing highly basic ligand frameworks, the 1e⁻-reduced Co^{I} species are nucleophilic enough to coordinate CO₂.[12] The CO₂ coordination to Co^{I} complex can be measured by the anodic shift of the half-wave potential (E$_{1/2}$) of the Co$^{II/I}$ redox couple under CO₂.[13]

A number of computational studies performed on these systems lead to a proposed general scheme (Scheme 1, *route i*) for either the electro- or photocatalytic CO_2-to-CO reaction based on two critical steps[5b,c,6b]: 1) CO_2 binding at the *in-situ* generated Co^I species to form a $Co^{III}CO_2$ adduct; and 2) the cleavage of the C-O bond. The latter step can be promoted by a second molecule of substrate to give free CO_3^{2-} in aprotic media (*route i.a*) or by protons (*route i.b*). The *route i.b* could take place through a stepwise electro/proton steps or eventhrough a proton couple electron transfer (PCET) reaction type with the formation of OH^- or water. On the other hand, for systems bearing less basic ligands, the CO_2 binding and catalytic conversion to CO might require the previous formation of a formal Co^0 intermediate, (Scheme 1, *route ii*).[8,9b,14]

C1 (S = H_2O)
-2.0 V, 93% FY_{CO+H2},
7.8 TON_{CO+H2}, 60 min

C2 (S = MeCN)
-2.1 V, 45% FY_{CO},
4.1 TON_{CO}, 40 min

C3
-2.0 V, 12% FY_{CO},
<1 TON_{CO}, 180 min

C4 (S = Me_2CO)
-2.8 V, 98% FY_{CO}, 6.2 TON_{CO},
120 min

C5 (S = H_2O)
-1.5 V, 94% FY_{CO}, 17 TON_{CO},
180 min

C6
-1.9 V, 60% FY_{CO},
5.0 TON_{CO}, 300 min

C7
-2.0 V, 22% FY_{CO},
3.7 TON_{CO}, 10 min

1
[$L^{N4}Co(OTf)_2$]
This work

Chart 1. Selected cobalt catalysts for electrochemical CO_2-to-CO reduction.[5c,8,9b,c,14-15] See Table S1 for further details.

In comparison to the C-O bond cleavage, the CO release step from the final Co^{II}-CO intermediate is generally considered facile and received much less attention (Scheme 1).[5b,c,8b] Nevertheless, recent spectroelectrochemical studies under CO_2, suggested that the formation of stable low oxidation state carbonyl complexes under CO_2 may result in the deactivation of the molecular transition metal catalysts. In particular, it was proposed that a Fe^0-CO species is formed in the course of the electrochemical CO_2 reduction by a quaterpyridine Fe complex.[8a] Analogous Ni^I-CO intermediates were detected for cyclam-type and aminopyridyl Ni complexes.[16] However, a direct observation of Co-CO intermediates formed during electrocatalytic CO_2 reduction is rare and mostly unexplored.[17]

Herein we present a compelling mechanistic study of the electrochemical CO_2-to-CO reduction mediated by a [$L^{N4}Co(OTf)_2$] (**1**) (L^{N4} = 1-[2-pyridylmethyl]-4,7-dimethyl-1,4,7-triazacyclononane) complex, recently studied for light-driven H_2 evolution[18] and organic substrates reduction[2a,19] (Chart 1). *In-situ* spectroelectrochemistry (SEC) studies reveal that a crucial and rarely reported cobalt(I) carbonyl species (**1$^{(I)}$-CO**) is formed under catalytic conditions at redox potential values of the $Co^{II/I}$ redox couple. Electrochemical and spectroscopic techniques (UV-Vis, FTIR, EXAFS

and NMR) were employed to characterize the reduced species observed under Ar and CO_2 atmosphere. These results together with DFT studies have served to present, for the first time, a full catalytic CO_2-to-CO cycle integrating the pH and redox potential effects. Additionally, we have explored the use of visible light as an effective strategy to induce the CO release from the Co-CO species improving the performance of CO_2 reduction catalysis. Finally, we propose a unified view of the CO_2-to-CO reduction mechanism under both electro- and photocatalytic conditions.

RESULTS AND DISCUSSION

Compound **1** has labile triflate ligands that exchange fast with coordinating solvent molecules to form the doubly charged CH_3CN complex (**1$^{(II)}$**), as characterized by X-ray diffraction (Figure 1). The two main features of the cyclic voltammogram of **1$^{(II)}$**, in anhydrous acetonitrile under argon atmosphere, are two irreversible waves; one at –1.74 V, assigned to a $Co^{II/I}$ process (potential values referenced *vs.* $Fc^{+/0}$ unless indicated)[19b], and the second one at -2.36 V, assigned to a formal $Co^{I/0}$ process (Figure 1, Figure S1).
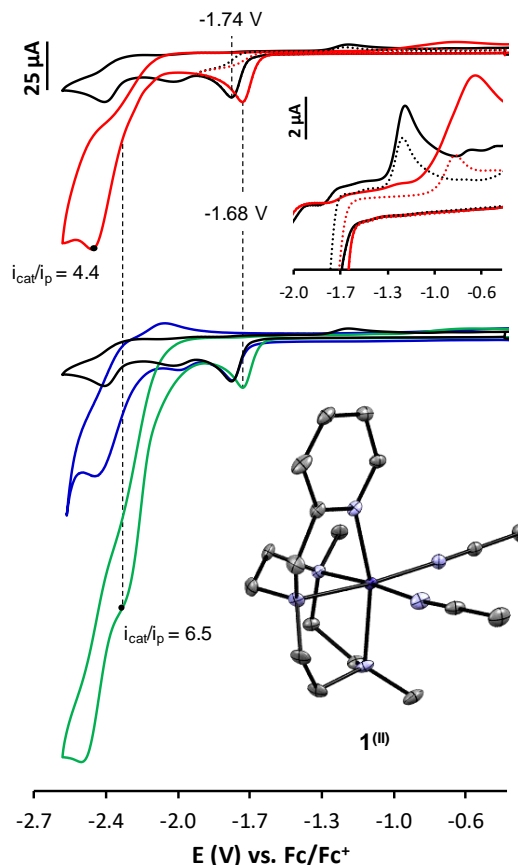
Figure 1. CVs of **1$^{(II)}$** (1 mM) in anhydrous $TBAPF_6$/CH_3CN (0.1 M) solution at v = 0.1 V·s^{-1}. **Top**) under Ar (black) and CO_2 (red); Inset: magnification range between -2.0 to -0.5 V. Scans window from –0.5 to –1.9 V are shown with dotted lines. **Bottom**) under Ar (black), and with added H_2O (0.55 M) under Ar (blue) and CO_2 (green). Inset: X-ray crystal structure of complex **1$^{(II)}$**, triflate counterions and hydrogen atoms have been omitted for clarity.

Under CO_2, the $Co^{II/I}$ peak potential shifts to positive values in terms of the CO_2 concentration; higher the substrate concentration larger the positive shift of the $E_p(Co^{II/I})$ value, reaching a maximum value of ΔE_p = 52 mV under CO_2 saturation ([CO_2] = 0.28 M). This is indicative of a fast reaction between the electrochemically generated Co^I species and CO_2 in the timescale of the CV experiment. In

addition, CO_2 saturation induces a small but significant current increase (25% in area) at the $Co^{II/I}$ wave in comparison with the CV under inert atmosphere (Figure 1, S2), suggesting that the process could not be described as mere coordination of CO_2 to the reduced Co^I species (Scheme 2). By reversing the potential just after the $Co^{II/I}$ couple, a small new oxidation peak at –0.82 V appears in the back scan, indicating the formation of a new species under CO_2 (Figure 1). The same anodic peak also appears under CO atmosphere, which suggests the formation of a common intermediate, most likely a cobalt carbonyl species (Figure S3, S4). Under CO, the $Co^{II/I}$ reduction wave shifts to even higher redox potentials (about twice than under CO_2, $\Delta E_p= 118$ mV). This behavior is a sign of a strong interaction between Co^I and CO, and on the order of previously reported in the literature.[8a,12d] Unfortunately, the irreversibility of the reduction wave prevents a precise calculation of the equilibrium constant (K_{CO}) by cyclic voltammetry (see section 3.1 in the SI). Nevertheless, we were able to obtain the kinetic binding constants ($k_{CO2} = 2\cdot10^3$ $M^{-1}s^{-1}$ and $k_{CO} = 6\cdot10^6$ $M^{-1}s^{-1}$) by applying equation 1, which relates the reduction potential peak E_p with the rate constant (k), the scan rate (v) and the substrate concentration (C).[8a]
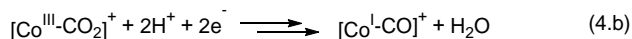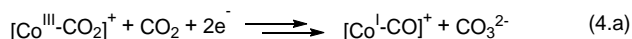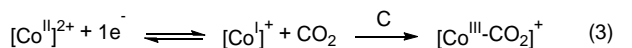
$$E_p = E^0_{1/2}\left(Co^{II/I}\right) - 0.78\frac{RT}{F} + \frac{RT}{2F}ln\frac{RTkC}{Fv}$$ (1)

Further reduction under CO_2 produces a catalytic wave at redox values close to the $Co^{I/0}$ process, reaching more than 4-fold current increase ($i_{cat}/i_p = 4.4$ at –2.42 V, Figure 1). Experiments at different catalyst and substrate concentrations indicate a 1st order catalytic reaction on either [$1^{(II)}$] and [CO_2] (Figures S7-S8).
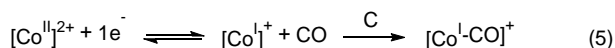
Under Ar

$$[Co^{II}]^{2+} + 1e^- \rightleftharpoons [Co^I]^+$$ (2)

Under CO$_2$

$$[Co^{II}]^{2+} + 1e^- \rightleftharpoons [Co^I]^+ + CO_2 \xrightarrow{C} [Co^{III}\text{-}CO_2]^+$$ (3)

$$[Co^{III}\text{-}CO_2]^+ + CO_2 + 2e^- \longrightarrow [Co^I\text{-}CO]^+ + CO_3^{2-}$$ (4.a)

$$[Co^{III}\text{-}CO_2]^+ + 2H^+ + 2e^- \longrightarrow [Co^I\text{-}CO]^+ + H_2O$$ (4.b)

Under CO

$$[Co^{II}]^{2+} + 1e^- \rightleftharpoons [Co^I]^+ + CO \xrightarrow{C} [Co^I\text{-}CO]^+$$ (5)

Scheme 2. Relevant reactions (a-d) in the cobalt-catalyzed CO_2 reduction. ET: electron transfer; C: chemical process.

The electrochemistry of $1^{(II)}$ in the presence of water (0.55-9.26 M) also gives some insight into the mechanism. Under Argon or CO_2, the presence of H_2O (0.55 M) did not produce any modification to the $Co^{II/I}$ reduction process (Figures 1 and S9), which implies that the proposed chemical reaction between the electroreduced cobalt complex and CO_2 is not significantly influenced by water (equation 3).[19b] However, at the catalytic wave the presence of water (0.55 M) induces a clear shift and current increase in both cases Ar and CO_2. Interestingly, controlled-potential electrolysis at this new catalytic wave under CO_2 and in presence of water shows an excellent CO/H_2 selectivity (no H_2 detected, 3.6 TON CO after 3 h at $E_{appl} = -2.37$ V, 0.5 M H_2O, Figure S10). This selectivity is remarkable considering that under Argon there is also an induced catalytic current by the presence of water at the same redox potential.

On the other hand, preparative-scale electrolysis of $1^{(II)}$ (1 mM, $E_{appl} = -2.46$ V) under a constant flow of CO_2 (30 mL min^{-1}) in anhydrous CH_3CN yields 5.5 TONs of CO after 6 h. This result provides evidence for catalytic CO_2 reduction even in the absence of an added proton source (Figure S11). Gas-chromatographic analysis (see experimental section in the SI) indicates that CO is the major product formed, along with the formation of carbonate. H_2

was not detected and formate was only detected in traces (TON $HCO_2^- \sim 0.1$). Rinse test study indicates that no deposit over the electrode was responsible for the main catalytic activity observed (Figure S12).

Spectroscopic and theoretical evidence for the formation of $1^{(I)}$-CO and $1^{(I)}$. The already mentioned current increase at the $Co^{II/I}$ reduction peak under CO_2 suggests further reactivity. To confirm this hypothesis, we employed *in-situ* spectroelectrochemical techniques[20] (UV-Vis-SEC, FT-IR-SEC) and spectroscopic characterization (^1H-NMR and EXAFS) of electrochemically generated intermediates by bulk electrolysis at the $Co^{II/I}$ reduction peak.
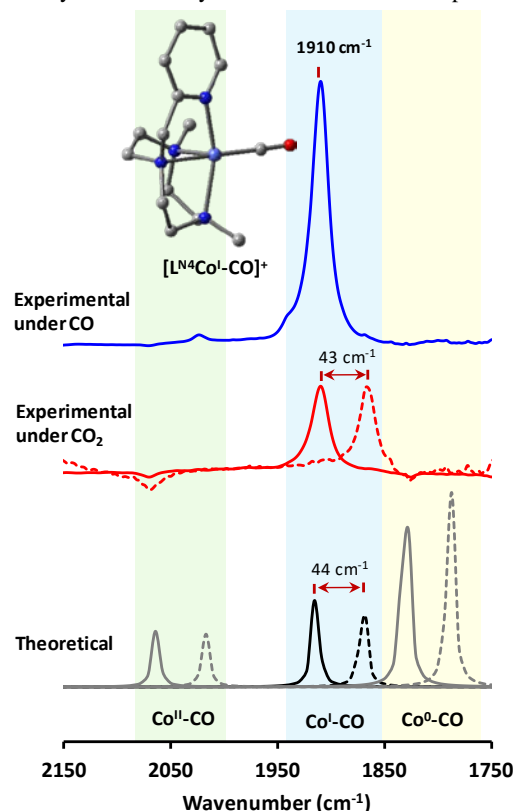
Figure 2. Top and middle: Experimental spectra obtained by FTIR-SEC of a 0.2 M TBAPF$_6$/CH$_3$CN solution of **1** (6 mM) under CO (blue) and CO_2 (red) at ca. –1.7 V ($^{12}CO_2$ plane, $^{13}CO_2$ dashed). Bottom: Theoretical ν_{CO} bands of $1^{(II)}$-CO, $1^{(I)}$-CO and $1^{(0)}$-CO ($^{12}CO_2$ red line, $^{13}CO_2$ dashed line) calculated at the B3LYP-D$_3$(SMD)/6-31+G* level of theory.

FTIR-SEC experiments in an OTTLE cell[21] revealed the formation of a new species at the first reduction event in a CO_2 saturated electrolyte. A stepwise scan to negative potentials showed the progressive formation of a new band ($\nu_{CO} = 1910$ cm^{-1}) when the applied potential reaches the first reduction peak (*ca.* –1.7 V, Figure S14). The same IR feature is also formed under CO, but about 3-fold more intense than under CO_2 (Figure 2, S15). Labeling experiments with $^{13}CO_2$ indicated that the detected intermediate derives from CO_2 reduction ($\nu^{13}_{CO} = 1866$ cm^{-1}, stretching band shifts 43 cm^{-1} towards lower energy). The observed vibration and isotopic shift are comparable to an uncommonly reported Co^I carbonyl complex. The direct reaction of the chemically synthesized [$L^{C1}Co^I$]$^+$ ($L^{C1}=$ 5,7,7,12,14.14-hexamethyl-l,4,8,11-tetraazacyclotetradeca-4,11-diene) with CO_2 leads to the formation of [$L^{C1}Co^I(CO)$]$^+$ after several days.[22] The [$L^{C1}Co^I(CO)$]$^+$ complex reported by E. Fujita *et al.* presents a ν_{CO} at 1916 cm^{-1} with a 47 cm^{-1} isotopic shift under $^{13}CO_2$.[22a]
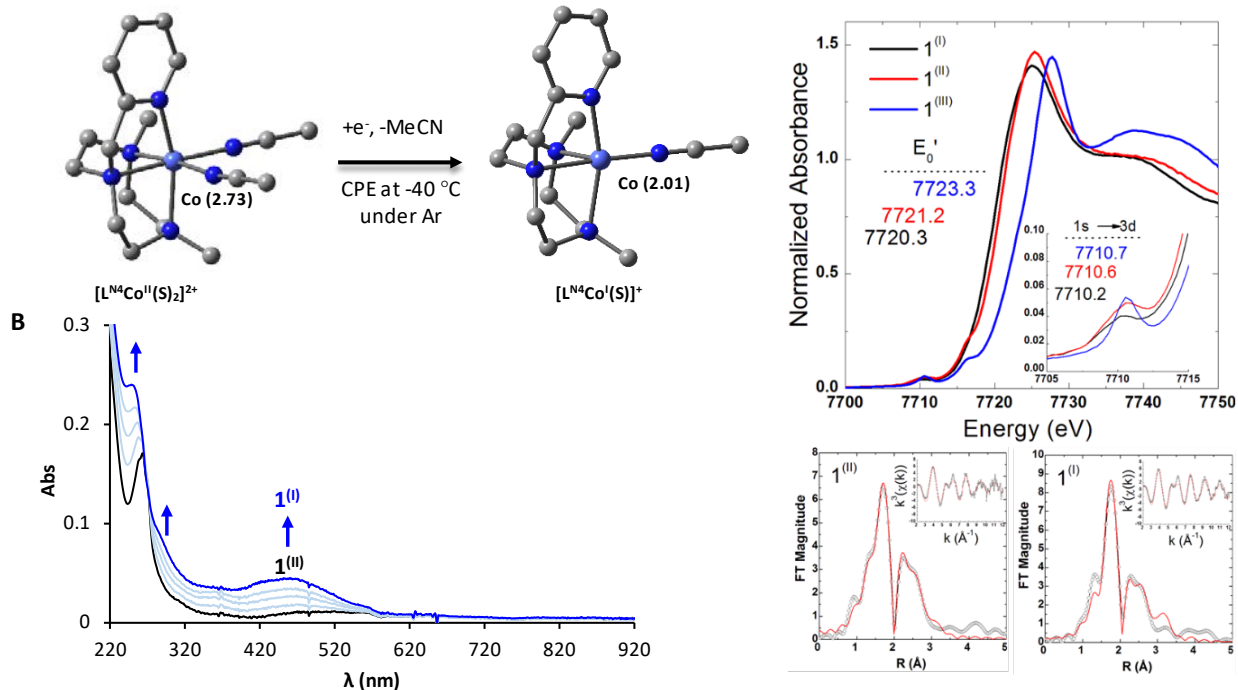
Figure 3. A) DFT (B3LYP-D$_3$/6-31+G*) modeled structures for the most stable Co^{II} ([L^{N4}Co^{II}(CH$_3$CN)$_2$]$^{2+}$) and Co^I ([L^{N4}Co^I(CH$_3$CN)]$^+$) species under the reaction conditions. The spin density over cobalt center is shown in parentheses. B) UV-Vis-SEC of **1$^{(II)}$** (black trace) at –1.7 V to yield a new reduced species (blue trace). C) Co K-edge XANES of complex **1** in I, II and III oxidation states with inset showing the pre-edge area of the 1s → 3d transitions. D) Fourier transformed EXAFS data and fits with the inset showing the k-space spectra (Data (circles) Fit (red)).

To further confirm the nature of the putative cobalt carbonyl intermediate, we computationally modeled the theoretical IR spectra of possible cobalt carbonyl species bearing the L^{N4} ligand, as well as known homoleptic cobalt carbonyl complexes (section 4.5 of the SI).[22b] This together with previously reported values,[12d] allowed us to discard homoleptic cobalt carbonyl complexes and other cobalt carbonyl complexes in oxidation state II and 0 bearing the L^{N4} ligand. The calculated 1912 cm^{-1} feature of [L^{N4}Co^I(CO)]$^+$ matches with the experimental ν_{CO} value of **1$^{(I)}$-CO** (1910 cm^{-1}) as well as with the theoretical ^{13}C shift (Figure 2).

Upon an oxidative back scan after the formation of **1$^{(I)}$-CO** in SEC under either CO$_2$ and CO atmosphere, the 1910 cm^{-1} feature of **1$^{(I)}$-CO** is preserved until about -0.8 V. Further oxidation leads to the disappearance of the **1$^{(I)}$-CO** signal recovering the original spectrum (Figures S12 B and S11 B, respectively). Then, the anodic peak at –0.8 V observed in the CVs under CO$_2$ and CO corresponds to the reoxidation of **1$^{(I)}$-CO**. Similar results were obtained under CO$_2$ in the presence water (0.5 M), showing a mixture of **1$^{(I)}$-CO** (ν_{CO} = 1910 cm^{-1}) and carbonate species (1676-1631 cm^{-1}) when the applied potential matches the Co$^{II/I}$ process (Figure S16).
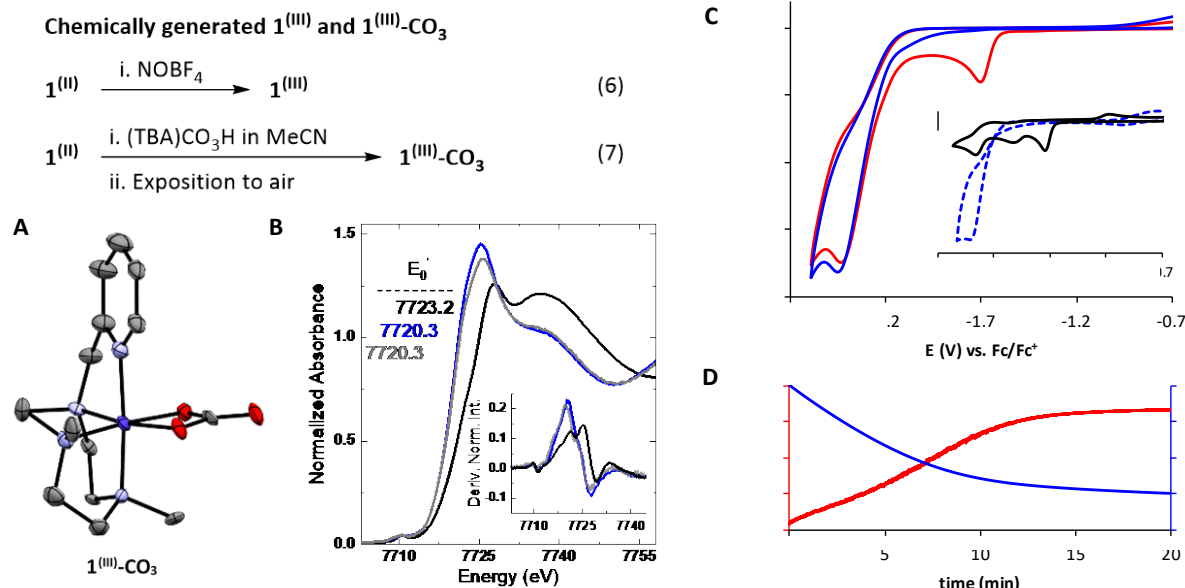
Altogether offers a compelling evidence for the formation of **1$^{(I)}$-CO** at the Co$^{II/I}$ redox potential through CO$_2$ reduction to CO. We propose that the formation of Co^I carbonyl species may be more general since we have also detected by IR spectroelectrochemistry the formation of [Co^I(tpa)(CO)]$^+$ (see section 3.6 of the SI). In addition, the formation of this carbonyl species is necessarily fast because it is detected in the CV time scale (Figure 1 inset).

UV-Vis-SEC experiments provided complementary information to FT-IR-SEC. Under Ar atmosphere, a new d-d transition band appears at λ_{max} 459 nm at the first reduction wave (ca. –1.9 V) (Figures

3 B, S17). The formation of the putative **1$^{(I)}$** is reversible, recovering **1$^{(II)}$** upon back scan oxidation.

Conversely, the reduction of **1$^{(II)}$** under CO$_2$-saturated conditions leads to the growth of two new bands at 308 and 427 nm, indicating the formation of a new species (Figure S18). In agreement with the CV data, these features disappear at an approximated applied potential of –0.8 V during the reverse sweep (Figure S19). In line with the above discussion, the same intense absorptions at 308 and 427 nm resulted from UV-Vis-SEC experiments under CO at the Co$^{II/I}$ potential, consistent again with the formation of **1$^{(I)}$-CO** (Figure S20). UV-Vis-SEC experiments are also interesting because they provide an estimation of the concentration of the species formed in solution. By analyzing the differences in absorbance values at 427 nm under CO$_2$ and CO, a 3-fold increase in the **1$^{(I)}$-CO** concentration is observed under CO relative to CO$_2$. This increase is comparable to that observed by FT-IR-SEC (Figure S21).

To explore the oxidation states and coordination geometries of the possible intermediates we performed Co K-edge XAS. The XANES profile is consistent with a centrosymmetric pseudo-octahedral coordination geometry (Figure 3C).[23,24] EXAFS analysis supports two coordination shells having 2 N/O scattering atoms at 2.0 Å and 4 N/O scattering atoms at 2.16 Å, which is consistent with the optimized DFT geometry (Figure 3 D and section 3.7 of the SI for details). To study the reduced species under Ar (Eq. 1) by XAS and EXAFS, we performed bulk electrolysis at -1.8 V of a solution containing **1$^{(II)}$** (5 mM, in anhydrous CD$_3$CN at –40 ºC under Argon). After 1e$^-$ passed, the solution was frozen and analyzed by Co K-edge XAS. The changes with respect to the Co K-edge XANES spectrum of **1$^{(II)}$** suggest the formation of a Co^I species **1$^{(I)}$** (Figure 3 C).

Chemically generated $1^{(III)}$ and $1^{(III)}$-CO$_3$

$$1^{(II)} \xrightarrow{\text{i. NOBF}_4} 1^{(III)} \quad\quad (6)$$

$$1^{(II)} \xrightarrow[\text{ii. Exposition to air}]{\text{i. (TBA)CO}_3\text{H in MeCN}} 1^{(III)}\text{-CO}_3 \quad\quad (7)$$

A $1^{(III)}$-CO$_3$

B

C

D

Figure 4. Chemical equations for the generation of $1^{(III)}$ and $1^{(III)}$-CO$_3$. A) ORTEP plot of the $1^{(III)}$-CO$_3$ X-ray crystal structure (see SI for structural parameters). B) Co K-edge XANES of the solution after CPE at –1.7 V (blue), the chemically generated references of $1^{(II)}$-CO$_3$ (grey) and $1^{(III)}$-CO$_3$ (black) with inset showing each first derivative. C) CVs of $1^{(II)}$ (1 mM) under CO$_2$ before (red) and after (red dashed) electrolysis at ca. –1.9 V. Inset: CVs under Ar (black) and under CO$_2$ in the presence of 1 eq. of TBACO$_3$H (blue dashed). D) Current and charge profiles along electrolysis of $1^{(II)}$ (1 mM) under CO$_2$. Electrolysis and CVs (0.1 V·s^{-1}) recorded in anhydrous TBAPF$_6$/CH$_3$CN (0.1 M) over carbon mesh and glassy carbon, respectively.

EXAFS analysis of the Co^I center shows a pentacoordinate environment (Figure 3A, D and section 3.7 of the SI). Nevertheless, XANES suggests a pseudo octahedral environment and DFT calculations show an almost isoenergetic penta/hexa-coordinate environments for Co^I, although it is prefered the pentacoordinated structure (the five-coordinate structure is 0.6 kcal·mol^{-1} more stable than its hexacoordinated counterpart). Therefore, we can postulate that although the pentacoordinate structure is preferred at room temperature, both pentan/hexa-coordination species could coexist (Scheme 3).
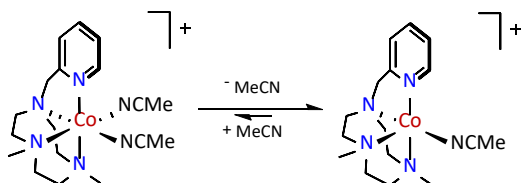
Scheme 3. Proposed penta/hexa coordination equilibrium of the electrochemically generated cobalt(I) species.

This is in agreement with the previously reported solid state structures of five-coordinate formal Co^I complexes based on polypyridine,[25] and pyridine-bisimine ligands.[14,23] The ^{1}H-NMR of the sample showed the formation of a new paramagnetic species is the range of 140 – 5 ppm at 235 K (Figure S26). The paramagnetic nature of the sample together with the DFT analysis of the $1^{(I)}$ spin density is consistent with a high-spin d^8 configuration of the metal center (Figure S27). Previous electronic structure studies of formal Co^I complexes with *N*-donor ligands are better described as Co^{II} with a reduced ligand, resulting in a challenging characterization of this naturally elusive intermediates. On the other hand, ligands with high crystalline-field splitting favor the formation of low spin Co^I complexes.[26] In this regard, the data presented herein are one of the few compelling evidence of the formation of a d^8 high-spin Co^I species reported so far.

While IR-SEC is an *in-situ* experiment that lasts seconds, the *ex-situ* bulk XAS experiment under CO$_2$ lasts at least 20 min prior to sampling an aliquot for analysis, which prevents the quantitative

accumulation of intermediates without decay. Nevertheless, we have performed CPE experiments under CO$_2$ analogous to the ones under argon. In this case, XAS shows a more effectively reduced metal center than the starting Co^{II} complex and distinct in bond metrics to the Co^I obtained under Ar (Figures 4 B, S35). Although we were not able to fit a short bond distance as expected for a Co-CO bond, the pre-edge intensity (0.04) as well as the pre-edge and rising edge energies (7710.3 eV;7720.4 eV) are similar to that of a Co^{II} carbonate reference ($1^{(II)}$-CO$_3$) generated by mixing $1^{(II)}$ with 1 eq. of tetrabutylammonium hydrogencarbonate (TBACO$_3$H). Furthermore, EXAFS analysis shows comparable bond metrics and coordination numbers in both the reference and electrochemically generated sample having 2N/O scattering atoms at 2.05 A and 4N/O scattering atoms at 2.16 A (Panel S1). In addition, upon deliberate exposition to ambient atmosphere, we generated a product that approaches the profile of the chemically generated Co^{III}-carbonate (Eq. 7), both in terms of XANES and EXAFS analysis. The new Co^{III}-carbonate species exhibits a diamagnetic ^{1}H-NMR spectrum, as expected for a low-spin d^6 metal center (Figure S29). X-ray diffraction of crystals obtained after electrolysis of $1^{(II)}$ under CO$_2$ confirmed the formation of a six-coordinate Co^{III} complex [L^{N4}Co^{III}(η^2-CO$_3$)](PF$_6$) ($1^{(III)}$-CO$_3$, Figure 4 A). In addition, electrolysis of $1^{(II)}$ (1 mM, at –1.7 V in anhydrous CH$_3$CN) under CO$_2$ produced CO over the first 20 minutes of reaction (Figure 4 D), consistent with the reduction of CO$_2$ through the $1^{(I)}$-CO formation pathway. Unfortunately, low-temperature bulk electrolysis at –40 ºC did not provide further evidence of the reactivity.

The formation of $1^{(III)}$-CO$_3$ species can be explained by the O$_2$ oxidation of *in situ* generated Co^{II}-carbonate species during the CO$_2$ reduction electrolysis (formally: 2CO$_2$ + 2e$^-$ $\rightarrow$ CO$_3^{2-}$ + CO). However, we cannot fully rule out that some of the carbonate is formed *via* CO$_2$ hydration since the water content in the solution is in the range of 40 – 60 ppm, as analyzed by Karl-Fischer titration under our conditions.[22a]

The sum of these results led us to hypothesize that the solution reaches a thermodynamic equilibrium, where the $1^{(I)}$-CO as well as the Co^{II} carbonate disfavor the catalytic CO$_2$ reduction at the Co$^{II/I}$ redox potential (Scheme S1). Indeed, the CV of the solution after

electrolysis of $1^{(II)}$ under CO_2 is consistent with the analogous CV in the presence of one equivalent of $TBACO_3H$ (Figure 4 C). The latter experiment also showed that at the $Co^{I/0}$ redox potential there is catalysis which implies that carbonate is not involved in the catalytic CO_2 reduction process.

Computational modeling of the mechanism. With the aim to give additional insight into the reactivity of electrochemically generated Co^I species with CO_2, we studied the reaction energy profile by DFT. The calculations were done at B3LYP-D_3(SMD) / aug-cc-pVTZ(-d^H,-$f^{C,N,O}$,-g^{Co}) // B3LYP-D_3(SMD) / 6-31+G* level, which reproduced well the catalytic activity of related systems.[19b] Computed Gibbs energies were corrected for the catalytic conditions, i.e. substrate (CO_2) and product (CO) concentrations of 0.28 M and 50 μM, respectively.[27] For a detailed description of the computational methodology and for the optimized structure coordinates see sections 4.1 and 6 of the SI.

In aprotic conditions, CO_2 is known to act as an oxide acceptor assisting the reductive disproportionation reaction to CO and CO_3^{2-}.[7b] Nevertheless, residual water contained in anhydrous CH_3CN may have an important role in the protonation of the cobalt-CO_2 adducts. To account for available protons, we studied the pH dependency of the mechanism. At the low proton concentration of reaction conditions, a proton assisted mechanism could be operative but competitive with an aprotic CO_2 reductive disproportionation mechanism. Therefore, in the first part of this section, we will discuss possible mechanisms for the formation of the key $1^{(I)}$-CO intermediate under both proton-assisted and aprotic conditions. Later, we will comment on the cobalt-catalyzed CO_2 reduction mechanism at the $Co^{I/0}$ redox potential focusing on the effect of the pH and the redox potential on the thermodynamics and kinetics of the catalytic reaction.

Formation of $1^{(I)}$-CO. According to the experimental data, the reduction of CO_2-to-CO occurs at the first $Co^{II/I}$ reduction wave (ca. –1.7 V), yielding $1^{(I)}$-CO and Co^{II}-carbonate species as the main reaction products. We have shown that, although the C-O bond cleavage can take place, the reaction does not proceed catalytically. In order to reproduce our experimental conditions at the $Co^{II/I}$ wave, the theoretical $Co^{II/I}$ reduction potential (-1.91 V) was chosen to calculate the energy profiles (Figure 5). As depicted in Figure 5 A, in the proton-assisted mechanism, the nucleophilic Co^I species ($[L^{N4}Co^I(S)]^+$) formed by 1e⁻ reduction of $[L^{N4}Co^{II}(S)]^{+2}$ binds CO_2 to form a higher in energy carboxylate adduct ($[L^{N4}Co^{III}-CO_2]^+$), with a 8.8 kcal·mol⁻¹ energy barrier. Then, the subsequent 1e⁻ reduction gives the slightly endergonic $[L^{N4}Co^{II}-CO_2]$ at the defined redox potential. Further protonation of the highly basic $[L^{N4}Co^{II}-CO_2]$ species yields the thermodynamically favored $[L^{N4}Co^{II}-CO_2H]^+$ ($pK_a = 28.4$).

The subsequent C-O bond cleavage step has been proposed as the rate determining step (r.d.s.) in the light-driven CO_2-to-CO reduction mechanism catalyzed by other macrocyclic Co complexes.[8b,28] In our case, the calculated Gibbs energy barrier for the heterolytic C-O bond cleavage from $[L^{N4}Co^{II}-CO_2H]^+$ to give $[L^{N4}Co^{II}-CO(OH)]^+$ is 16.0 kcal·mol⁻¹ (Figure 6A). This result is in agreement with the previously reported data for complex C6 and its variants showed in Chart 1.[5c]

However, we found that even at the low proton concentration given by 0.4 μM of water, the C-O bond cleavage triggered *via* a second protonation of $[L^{N4}Co^{II}-CO_2H]^+$ (Figure 5 A) is kinetically more favored ($\Delta G^{\ddagger}_{1st CO2} = 12.2$ kcal·mol⁻¹). The subsequent release of a water molecule to form $[L^{N4}Co^{II}-CO]^{2+}$ is entropically driven due to the low concentration of water in organic solution. Likewise, the recovery of the starting $[L^{N4}Co^{II}(S)]^{2+}$ could be formed by the CO release from $[L^{N4}Co^{II}-CO]^{2+}$ which would complete the first turnover cycle. The rate determining step of this postulated catalytic cycle is the proton-assisted C-O bond cleavage with a kinetic barrier

as low as $\Delta G^{\ddagger}_{1st CO2} \sim 12.2$ kcal·mol⁻¹, which is kinetically feasible at room temperature. However, at a higher proton concentration (pH < 24.5), the kinetics will be independent of the protonation events and governed by the CO_2 binding step ($\Delta G^{\ddagger}_{binding}= 8.8$ kcal·mol⁻¹).

At this point, our modeled 2e⁻ reduction mechanism, that catalyzed the $CO_2 + 2H^+$ reduction to CO + H_2O by $1^{(II)}$, is similar to the recently proposed mechanisms for similar systems under both photo- and electrochemical conditions.[5c,29] However, none of the previously reported mechanisms gives an explanation for the general non-catalytic behavior of these systems at the $Co^{II/I}$ wave. Indeed, according to the Co^{II}/Co^{II}-CO mechanism, $1^{(II)}$ should catalyze the CO_2-to-CO reduction at the $Co^{II/I}$ reduction potential with fast reaction rates due to its low kinetic barrier. Nonetheless, we have shown that our cobalt complex is not catalytic within the CV timescale (100 mV/s) at the $Co^{II/I}$ wave, and only substoichiometric amounts of CO were accumulated during corresponding electrolysis experiments. Furthermore, we identified the formation of $1^{(I)}$-CO, which is yet to be included as an intermediate in the CO_2-to-CO reduction catalyzed by aminopyridine cobalt complexes.[7b]

In order to account for a model that fits our experimental observations, we considered the further reduction of the cobalt-based intermediates involved in the CO_2 reduction mechanism. In this regard, it is remarkable that the 1e⁻ reduction of $[L^{N4}Co^{II}-CO]^{2+}$ is highly favored at the $Co^{II/I}$ reduction potential ($E_{1/2}(Co^{II/I}$-CO) = –0.94 V; $\Delta G(Co^{II/I}$-CO) = –22.3 kcal·mol⁻¹). Then, $[L^{N4}Co^I-CO]^+$ becomes the most stable intermediate of the Gibbs energy profile. Indeed, the strong Co-CO bond is responsible for this stability with respect to Co^I. The nature of the CO binding and its π-backbonding character can be illustrated by the frontier molecular orbital analysis in the Co^{II}, Co^I and formal Co^0 oxidation states (Figure S36). In the case of Co^{II}-CO, there is not a significant π-backdonation from the Co center to the CO ligand, as it is expected for an electron poor metal center. However, regarding Co^I-CO and Co^0-CO, two of the β singly occupied d orbitals of $Co^{I/0}$ contribute to the π-backbonding character of the Co-CO bond as it is shown by the canonic orbitals depicted in Figure 6 B. Moreover, the enhanced stability in $[L^{N4}Co^I-CO]^+$, provided by the presence of a π-acceptor ligand, can be explained by means of the 18 e⁻ counting rule. While the CO release from Co^{II} (17 e⁻) is exergonic, the release from Co^I (18 e⁻) is highly endergonic ($\Delta G_{CoI-CO} > 20.2$ kcal·mol⁻¹) which prevents catalysis at the $Co^{II/I}$ redox potential. Similarly, the CO release from Co^0-CO is endergonic by 24.3 kcal·mol⁻¹. Indeed, the electronic structure of the formal Co^0-CO is better described as $[(L^{N4})^{\cdot-}Co^I-CO]$ (18 e⁻) since the β-HOMO orbital is mainly delocalized in the pyridine ring with a small contribution of the metal center.

According to the energetic span model, the overall kinetic barrier of a catalytic process (δE_{span}) should be calculated as

$$\delta E_{span} = \begin{cases} G_{TDTS} - G_{TDI} & TDTS\ after\ TDI \\ G_{TDTS} - G_{TDI} + \Delta G_r & TDTS\ before\ TDI \end{cases} \quad (8)$$

where G_{TDI}, G_{TDTS} and ΔG_r correspond to the Gibbs energies of the TOF Determining Intermediate (TDI), the TOF Determining Transition State (TDTS) and the reaction, respectively.[30] In our case, the TDI corresponds to the $[L^{N4}Co^I-CO]^+$ intermediate, and at a working potential of –1.91 V, the TDTS is $[L^{N4}Co^{II}-CO\cdots OH_2]^{2+}$. Then, the energy barrier of the catalytic process is given by δE_{span} = $\Delta G([L^{N4}Co^{II}-CO_2H]^+)$ + $\Delta G([L^{N4}Co^I-CO])$ + ΔG_r = 30.3 kcal·mol⁻¹. The kinetic barrier of the catalytic cycle includes the CO release from the TDI ($\Delta G_{release}$) to recover the active species and the energy barrier of the first CO_2 activation ($\Delta G^{\ddagger}_{1st CO2}$). Conversely to $\Delta G^{\ddagger}_{1st CO2}$, δE_{span} exceeds the kinetic limit for a catalytic process at room temperature. Furthermore, this model is in agreement with the accumulation of $1^{(I)}$-CO at ca. –1.7 V evidenced by thin layer SEC (*vide supra*).
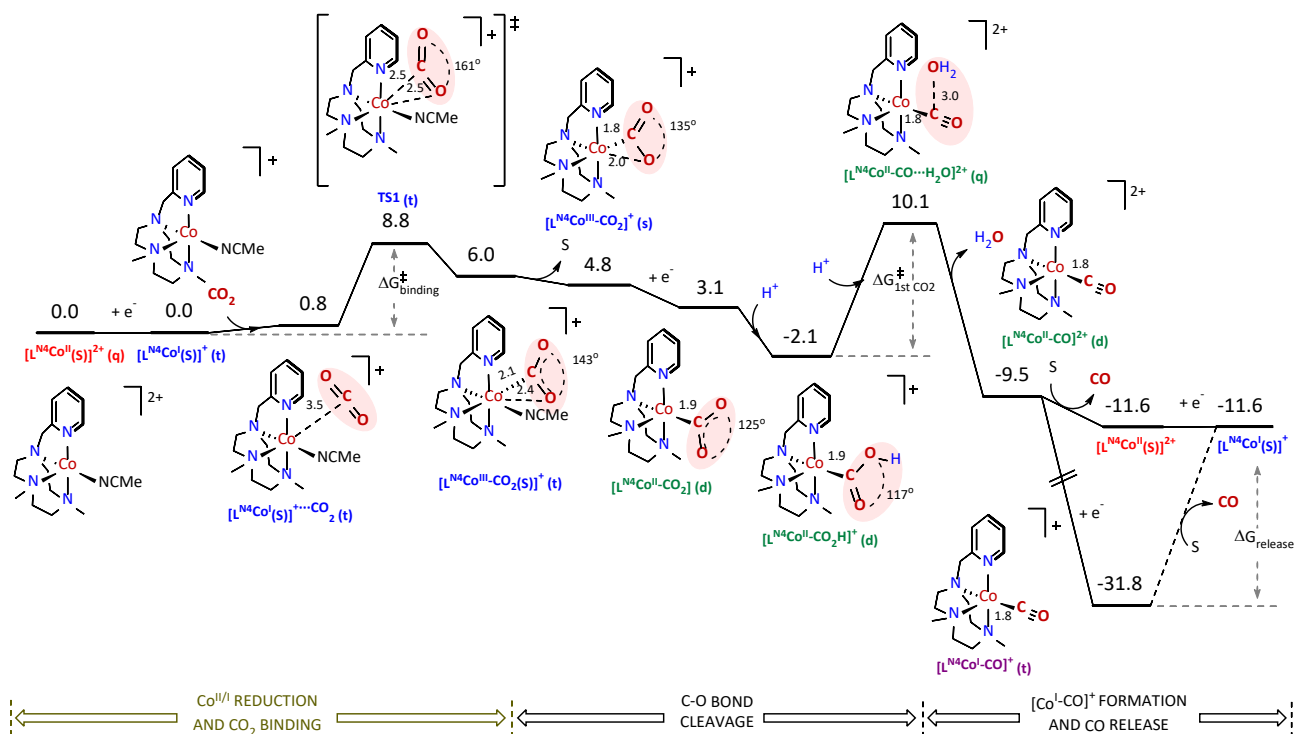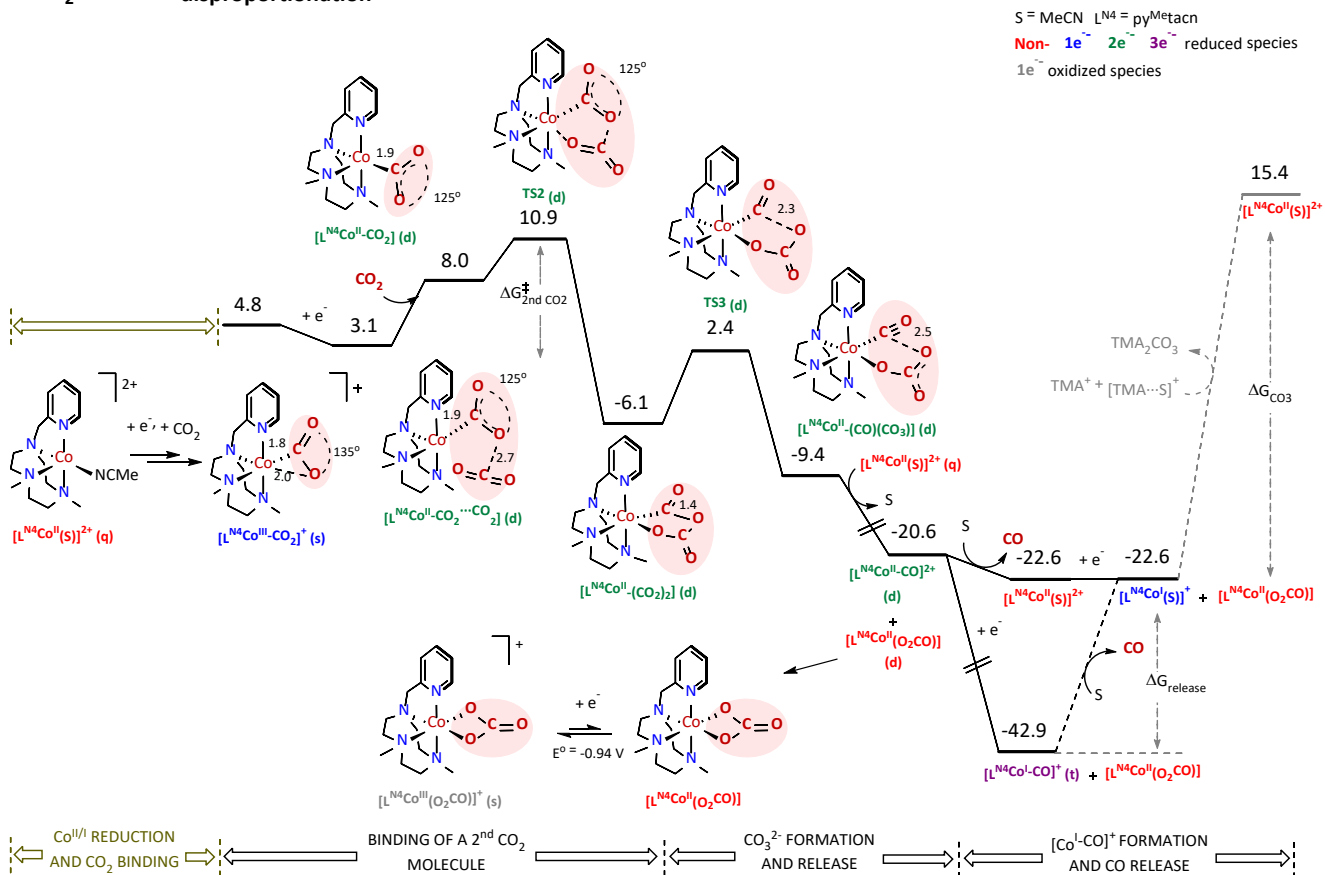
**Figure 5.** Computed Gibbs energy profile for the $[L^{N4}Co^I\text{-}CO]^+$ formation through the CO_2 reduction to CO mediated by $1^{(II)}$ at a working potential of -1.91 V *vs.* Fc/Fc^+ and pH 25. Energies and other relevant thermodynamic and structural parameters are given in kcal·mol^{-1}, V *vs.* Fc/Fc^+, Å and degrees. The spin multiplicity of each intermediate is shown in parenthesis: singlet (s), doublet (d), triplet (t), quartet (q). TMA = tetramethylammonium.
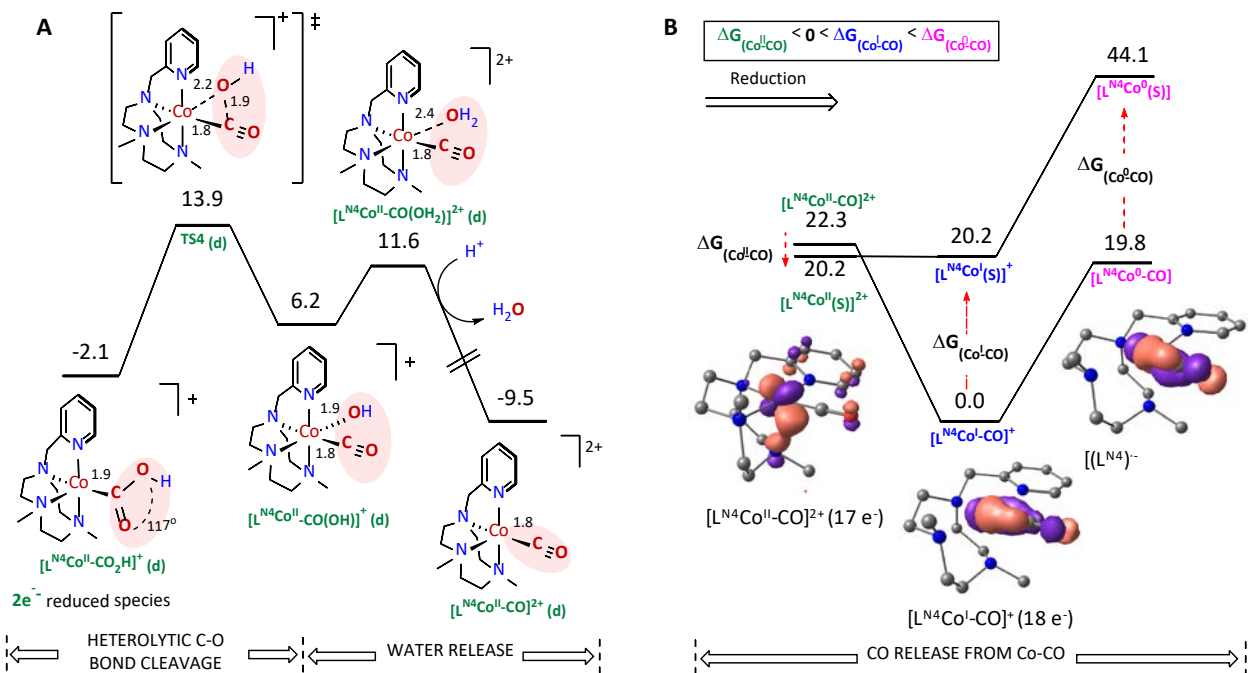
Figure 6. A) Heterolytic C-O bond cleavage step starting from $[\mathbf{L^{N4}Co^{II}\text{-}CO_2H}]^+$ to form $[\mathbf{L^{N4}Co^{II}(CO)(OH)}]^+$ intermediate. B) Thermodynamics of the $Co^{II/I/0}$ one electron reductions and each corresponding CO release step. Selected singly occupied molecular orbital of $Co^{II/I/0}$-CO complexes (isovalue 0.07). Energy profiles computed at -1.91 V *vs.* Fc/Fc^+ and pH 25.

Alternatively, the reductive disproportionation mechanism has been also computed to explain the formation of $\mathbf{1^{(I)}\text{-}CO}$ in the absence of H^+ (Figure 5 B). In this case, after the first CO_2 binding, another CO_2 molecule binds to $[\mathbf{L^{N4}Co^{II}\text{-}CO_2}]^{2+}$ to form the thermodynamically downhill $[\mathbf{L^{N4}Co^{II}\text{-}(CO_2)_2}]^{2+}$ with a kinetic barrier of 10.9 kcal·mol^{-1}. The subsequent C-O bond cleavage to obtain a $[\mathbf{L^{N4}Co^{II}\text{-}(CO)(CO_3)}]^{2+}$ is exergonic and proceeds with a barrier of 8.5 kcal·mol^{-1}. Then, a second Co^{II} molecule can assist the release of carbonate to form $[\mathbf{L^{N4}Co^{II}(O_2CO)}]$ and $[\mathbf{L^{N4}Co^{II}\text{-}CO}]^{2+}$, which reduction at working potential is strongly exergonic (equation 9). Therefore, the $\mathbf{1^{(I)}\text{-}CO}$ formation through the disproportionation mechanism has a lower Gibbs energy barrier than in the proton assisted mechanism at pH values higher than 25.3.

On the contrary, the energy span for the reductive disproportionation mechanism ($\Delta G^{\ddagger}_{2nd\,CO2} + \Delta G_{release} + \Delta G_{CO3} = 69.2$ kcal·mol^{-1}) is by far higher than in the proton assisted mechanism due to the additional stability of the Co^{II}-carbonate species.

$$\begin{array}{c} [\mathbf{L^{N4}Co^{II}\text{-}CO(CO_3)}] \\ + \\ [\mathbf{L^{N4}Co^{II}\text{-}NCMe}]^{2+} \end{array} \xrightarrow{-\ MeCN} \begin{array}{c} [\mathbf{L^{N4}Co^{II}\text{-}CO}]^{2+} \\ + \\ [\mathbf{L^{N4}Co^{II}(CO_3)}] \end{array} \quad (9)$$
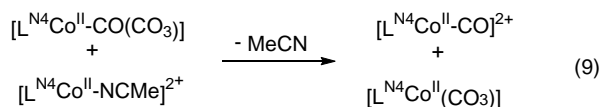
These results clearly show that the formation of $\mathbf{1^{(I)}\text{-}CO}$ is both thermodynamically and kinetically favored. The high stability of $\mathbf{1^{(I)}\text{-}CO}$ and the partial sequestration of the starting Co^{II} in the form of cobalt carbonate kinetically prevents the catalytic CO_2 reduction at the $Co^{II/I}$ redox potential, in agreement with the detection of $\mathbf{1^{(I)}\text{-}CO}$ and cobalt carbonate species in solution after electrolysis. Both theoretical and experimental results highlight the complexity of the cobalt catalyzed CO_2 reduction mechanism. As it has been shown, δE_{span} strongly depends on the stability of $\mathbf{1^{(I)}\text{-}CO}$ but also on redox and protonation events which are controlled by the applied redox potential and the pH of the medium, respectively. Indeed, the variation of these two factors can switch the operative mechanism for the formation of $\mathbf{1^{(I)}\text{-}CO}$ from a pH-independent reductive disproportionation mechanism to a proton assisted CO_2 reduction mechanism.

Catalytic CO_2 reduction. According to cyclic voltammetry, further reduction to formal Co^0 intermediates is needed in order to activate the catalytic process. Moreover, the catalytic wave increases in current when H_2O is added to the solution and it shifts to more positive potentials. Therefore, we have evidence to support that catalysis is assisted by the presence of H^+. As above shown, the catalytic wave it is not affected by the presence of added carbonate, and then it can be excluded from the mechanism. These experimental evidence, together with the previous DFT study, led us to hypothesize a reaction mechanism in which: i) first $[\mathbf{L^{N4}Co^{I}\text{-}CO}]^+$ is reduced to the formal $[\mathbf{L^{N4}Co^{0}\text{-}CO}]$ ($E_{1/2}(Co^{0/I}) = -2.77$ V, Figure 7 A); ii) and then a second CO_2 binding occurs forming the corresponding carboxylate adduct $[\mathbf{L^{N4}Co^{II}\text{-}CO_2(CO)}]$. Thereafter, protonation and further 1e$^-$ reduction yields $[\mathbf{L^{N4}Co^{I}\text{-}CO_2H(CO)}]$. At this point, a second protonation breaks the C-O bond forming the $[\mathbf{L^{N4}Co^{I}\text{-}(CO)_2}]^+$ intermediate by the extrusion of a water molecule. In contrast with the mechanism described in Figure 5, the CO release from $[\mathbf{L^{N4}Co^{I}\text{-}(CO)_2}]^+$ is thermodynamically favored, and the 18 e$^-$ intermediate $[\mathbf{L^{N4}Co^{I}\text{-}CO}]^+$ is recovered closing a catalytic cycle.

We have evaluated how the thermodynamics (ΔG_r) and kinetics (δE_{span}) of the catalytic process are modified in terms of both the redox potential and pH. Although this type of analysis has its precedents in heterogeneous catalysis, it is uncommon in the study of molecular systems.[31] The variation of the redox potential and pH not only changes the kinetic barrier, but also determines which species play the key role of TDTS and TDI. To facilitate the study of the change of the mechanism of a reaction in terms of redox potential, pH and concentration of the chemical compounds, we have developed a software tool that identifies the TDI and TDTS and calculates δE_{span} and ΔG_r as a function of these variables. The summary of the resulting analysis for the CO_2-to-CO catalyzed by $\mathbf{1^{(I)}\text{-}CO}$ is shown in Figure 7.

8
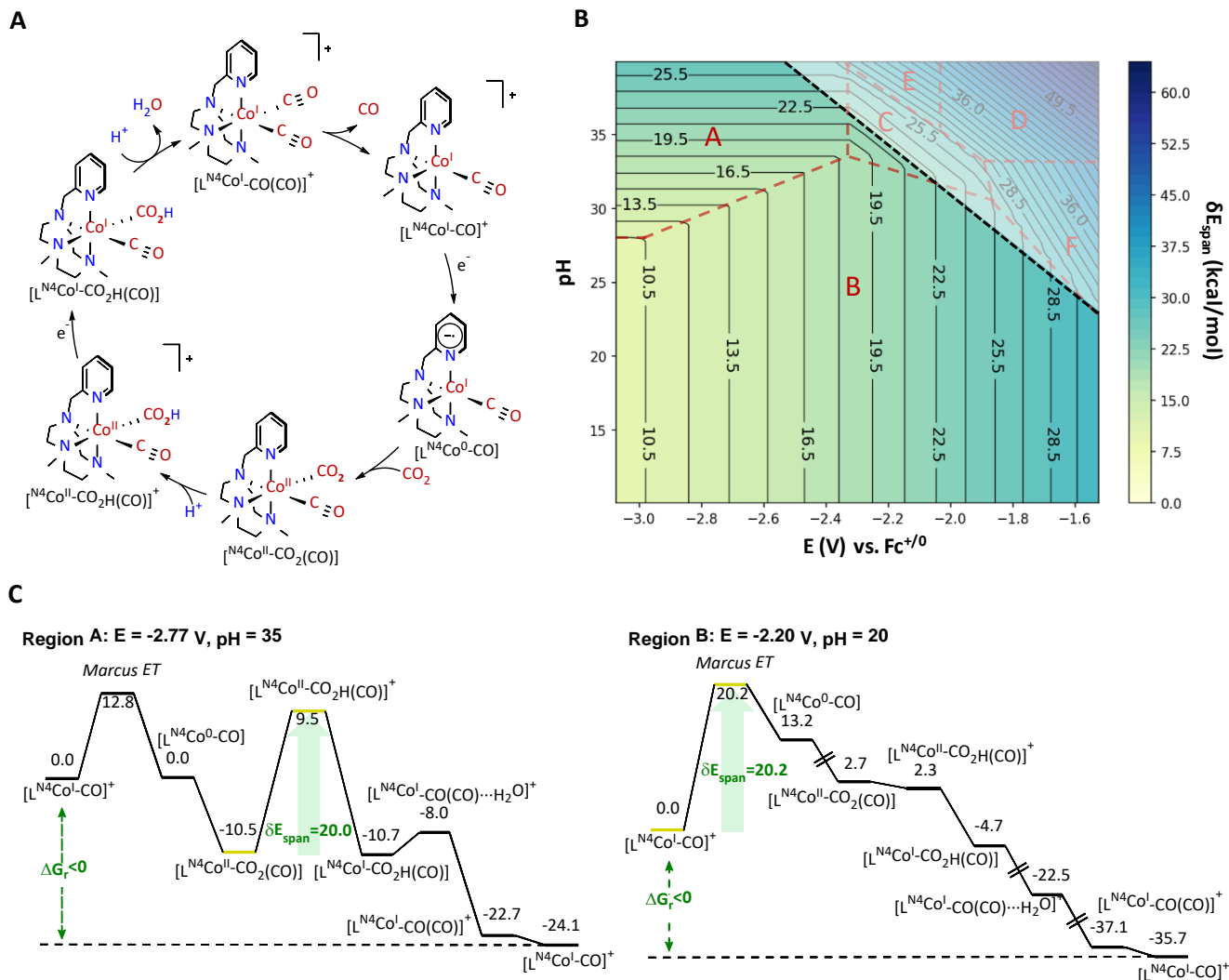
Figure 7. A) Proposed reaction mechanism for the CO₂ reduction to CO catalyzed by **1^(I)-CO**. B) Contour-plots of the kinetic energy span δE_span (color scale, kcal·mol⁻¹) of the calculated reaction mechanism *versus* the applied reduction potential (horizontal axis, V *vs.* Fc/Fc⁺) and the pH (vertical axis). Regions A-F are delimited by dashed red lines and the dashed black line spares the thermodynamic (ΔG_r < 0 kcal·mol⁻¹) regime from the non-thermodynamic one (ΔG_r > 0 kcal·mol⁻¹). C) Gibbs energy profiles associated with Regions A and B.

In order to illustrate the variation of the reaction kinetics in Figure 7, the δE_{span} value is represented by a color scale in a contour plot, where the vertical and horizontal axes correspond to the pH and redox potential (E vs. Fc⁺/⁰), respectively. In the resulting 2D map, we can identify regions where the kinetics either depend on the pH (A), on the redox potential (B), or on both pH and redox potential (C-F). The black dashed line in the 2D map represents the pH and redox potential values with $\Delta G_r = 0$ for the catalytic cycle. For simplicity, we will focus on regions A, B and C, as they are the ones where the reaction mechanism is thermodynamically favored (ΔG_r < 0 kcal·mol⁻¹, Figure S42). The Gibbs energy profiles of regions E-F are given in Figure S43.

Region A corresponds to a regime where the redox potential is more negative than –2.3 V and the concentration of protons is very low. According to the corresponding energy profile (Figure 7 C), the 1e⁻ reduction of **[L^N4Co^I-CO]⁺** to form **[L^N4Co⁰-CO]** presents a non-negligible kinetic barrier. However, the formal Co⁰ species is reactive enough to bind CO₂ forming **[L^N4Co^II-CO₂(CO)]** *via* a barrierless reaction, unlike in the case of Co^I where the CO₂ binding is endergonic and with a barrier of 8.8 kcal·mol⁻¹ (Figure 5). The following protonation of **[L^N4Co^II-CO₂(CO)]** to form **L^N4Co^II-CO₂H(CO)]⁺** becomes the rate-determining step of the reaction.

9

For instance, at pH 35 and E < –2.35 V the δE_{span} determined by this step is 20.0 kcal·mol⁻¹. As anticipated above, further reduction and protonation yields **[L^N4Co^I-(CO)₂]⁺** together with the extrusion of a water molecule. Finally, CO is thermodynamically favorable released to recover the key **[L^N4Co^I-CO]⁺** intermediate.

As it can be inferred from the 2D plot, the increase in the proton concentration will drive the reaction to region B. Once in region B, the reaction rate is given by the Co^I/⁰ electron transfer process. That is why we have included the Marcus electron transfer barrier to better describe the reaction kinetics of this step. Then, as δE_{span} solely involves an electron transfer, the reaction rate only depends on the reduction potential. The subsequent CO₂ binding, protonation and reduction steps are thermodynamically favored, and the overall energy profile becomes downhill in Gibbs energy. For instance, at –2.35 V and pH < 33 the δE_{span} is 18.0 kcal·mol⁻¹. Finally, in region C the kinetic barrier depends on the Co^I/⁰ thermodynamics and also on the kinetics of the protonation of the carboxylate adduct **[L^N4Co^II-CO₂(CO)]** (Figure S43).

In summary, our model allows for the rationalization of the experimental observations. First, it describes a regime where the catalytic reaction is kinetically unfavorable at low overpotentials and

high pH values. This data is also in agreement with the lack of catalytic current at the $Co^{II/I}$ redox potential, even upon addition of water to the reaction media, and with the detection of Co^I carbonyl species. In addition, our model gives an explanation of the peak shift and current increase measured by CV at the $Co^{I/0}$ redox potential in the presence of water (*vide supra*).

The mechanistic proposal for the CO_2 reduction at the $Co^{II/I}$ redox wave suggests that catalysis could be activated by avoiding the $1^{(II/I)}$-CO reduction. However, we noticed that this 1e⁻ reduction is much more favored than the $Co^{II/I}$ process. Therefore, under electrochemical conditions the formation of $1^{(I)}$-CO is difficult to avoid.

A beneficial strategy to facilitate the metal carbonyl labilization is the use of photocatalysis since it can operate at very low concentrations. For bimolecular catalysis/photosensitizer reactions, at very low concentrations the electron transfer rate is under diffusion control. Therefore, at low enough catalyst concentration, the $1^{(II/I)}$-CO reduction rate could be lower than the CO release allowing the Co^{II}/Co^{II}-CO mechanism. Another beneficial strategy to promote catalysis could be based on the metal carbonyl labilization. In this regard, photocatalysis can facilitate it. It is well-known that light induces the M-CO bond cleavage in organometallic carbonyl species.[32]

Catalysis and the effect of light irradiation. With the aim of testing our hypothesis, we designed the following experiments to promote catalysis at the $1^{(II/I)}$ redox couple *via* the Co^{II}/Co^{II}-CO mechanism.

We studied $1^{(II)}$ as a homogeneous catalyst for the light-driven CO_2 reduction in combination with two different cyclometalated Ir photosensitizers. The typically used $[Ir^{III}(ppy)_3]$ (PS_{Ir1}) with an $E_{1/2}(PS_{Ir1}^{0/-})$ redox potential of –2.67 V, low enough to promote the reduction of $1^{(I/0)}$-CO and $[Ir^{III}(ppy)_2(bpy)](PF_6)$ (PS_{Ir2}), with a $E_{1/2}(PS_{Ir2}^{+/0})$ of –1.78 V at which the formation of $1^{(0)}$-CO is not accessible (Figure 8). Experiments were performed with $1^{(II)}$ (50 µM) and the photosensitizer (200 µM) in CO_2 saturated CH_3CN:Et_3N mixed (4:1 v/v) irradiated at 447±20 nm for 24 h at 25 °C. Gases evolved were quantified by GC, with CO and H_2 as the only detected products (Figures 9, S44). Remarkably, although PS_{Ir2} provides a redox potential 820 mV less negative than PS_{Ir1}, both photosensitizers result in a similar reaction rate and catalytic activity (TON of CO 69±2 and 68±3 for PS_{Ir1} and PS_{Ir2}, respectively). These data confirmed that the *in-situ* generated Co^I species is able to promote a selective conversion of CO_2-to-CO as anticipated from the electrochemical and computational studies. DLS analysis indicates that nanoparticles are not responsible for the main catalytic activity observed (Figure S45).

On the other hand, in an attempt to avoid the CO-poisoning process under electrochemical conditions, we also performed electrolysis experiments under blue light irradiation. Previous studies by T. C. Lau, M. Robert and co. suggested that light irradiation could indeed facilitate the CO release in the case of the $[Fe^I(qpy)CO]^+$ adduct over the reduction to Fe^0 carbonyl species.[8a] For these set of experiments, we carefully controlled the reaction temperature (25 ºC) with a jacketed electrochemical cell connected to a cryostat. CV of $1^{(II)}$ under blue LED light (447±20 nm) in CO_2-saturated solution showed the disappearance of the reoxidation peak at –0.8 V (Figure S46).[10] This feature is reproducible upon successive switch on/off cycles.
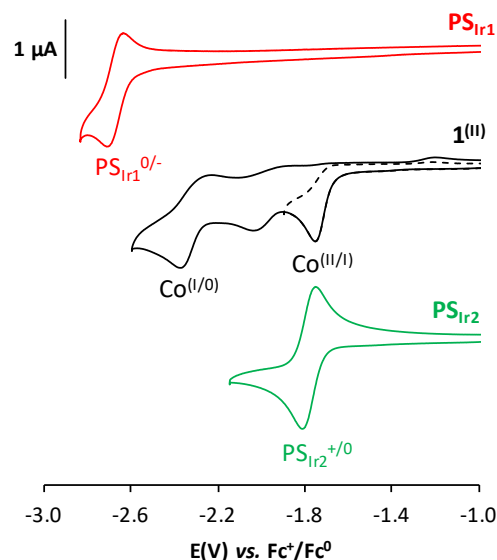
Figure 8. CVs of $1^{(II)}$ (black), PS_{Ir1} (red) and PS_{Ir2} (green) at 0.5 mM concentration in anhydrous TBAPF$_6$/CH$_3$CN (0.1 M) solution. $v = 0.1$ V·s⁻¹, $\emptyset = 0.1$ cm.
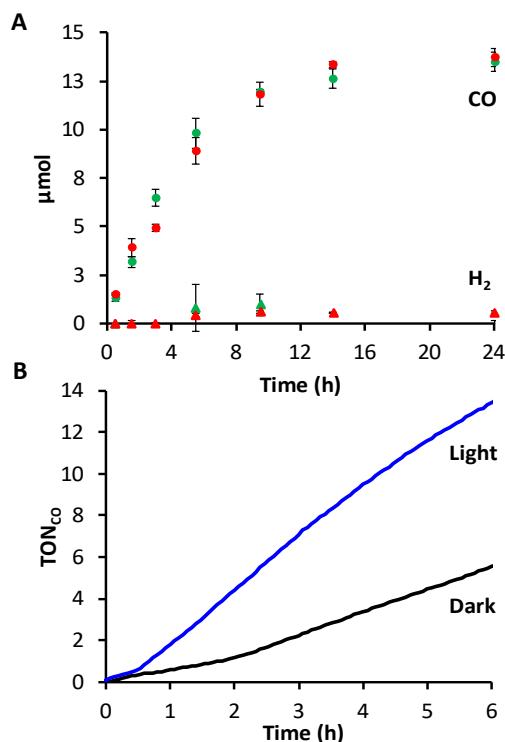
Figure 9. A) CO (circles) and H_2 (triangles) evolution under photocatalytic conditions ($[1^{(II)}] = 50$ µM, [PS] = 0.2 mM, 4:1 v/v CH$_3$CN:Et$_3$N, $\lambda_{LED} = 447$ nm). PS_{Ir1} (red) and PS_{Ir2} (green) were used as photosensitizers. B) TON of CO over time under bulk electrolysis conditions (1 mM of $1^{(II)}$ in 0.1 M TBAPF$_6$/CH$_3$CN under CO_2 at $E_{appl} = -2.46$ V in the dark (black trace) and under irradiation (blue trace).
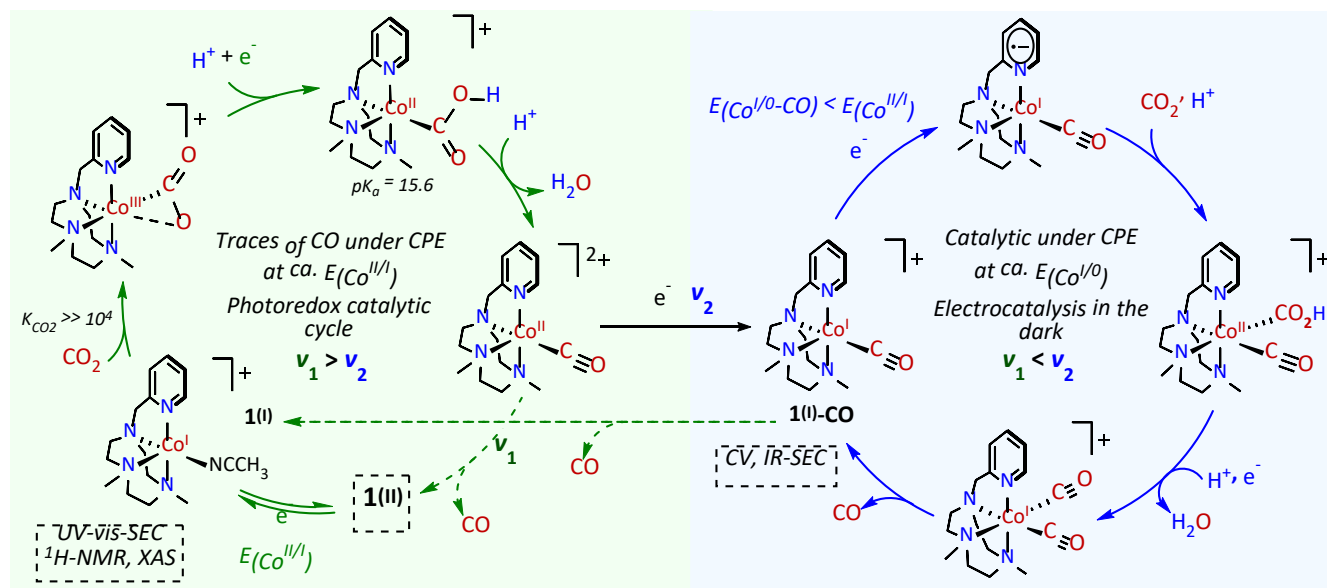
Scheme 4. Proposed unified mechanism for photo- and electrochemical CO_2 reduction catalyzed by $1^{(II)}$ with relevant catalytic intermediates based on experimental evidence (dotted boxes) and DFT calculations.

When a constant E_{appl} potential of –2.46 V is held for 6 h under irradiation a substantial improvement of the catalytic activity of $1^{(II)}$ is observed ($TON_{CO} = 13$, $FY_{CO} = 38\%$) with respect to the performance in dark ($TON_{CO} = 5.5$, $FY_{CO} = 26\%$), in terms of both catalytic turnovers and faradaic yield for CO production (Figure S47). Prolonged electrolysis highlights a sustained electrocatalytic current, leading to almost 20 turnovers of CO after more than 10 h and maintaining the same average efficiency. This is consistent with a beneficial effect of blue-light photoirradiation on catalysis, consisting of a light-induced cleavage of the accumulated stable Co-CO species in solution, thus favoring a partial regeneration of the catalyst. On the other hand, the effect of irradiation is barely observed during light-assisted electrolysis at –1.70 V under CO_2 atmosphere, suggesting a smaller effect of light absorption on the $1^{(I)}$-CO species (Figures S49 and Table S18).

A unified photo- and electrochemical CO_2 reduction mechanism. Gathering together all studies, in Scheme 4 we present in a simplified manner our proposal for the most likely pathways for the $2e^-$ photocatalytic and electrocatalytic CO_2 reduction to CO and the connections between them. In this study, we show that the formation of a very stable metal carbonyl under electrocatalytic conditions is detrimental for the catalyst turnover. At the end of the first catalytic cycle, the catalysis is interrupted by the formation of $1^{(I)}$-CO. However, this is not the case under photocatalytic conditions, which is able to reduce CO_2 to CO at a redox value as low as -1.78 V. As it is shown in Scheme 4, the main difference between the electrocatalytic and photocatalytic conditions is the competition between the formation of $1^{(I)}$-CO (v_2) and CO release (v_1) both from $1^{(II)}$-CO. Under electrochemical conditions, the fast $1^{(II/I)}$-CO reduction by the electrode surpasses the CO release, producing $1^{(I)}$-CO. Then, in electrocatalytic conditions, the catalysis is only achieved when system is forced to evolve towards low valent carbonyl species ($Co^{I/0}$ blue cycle, Scheme 4). Instead, under photocatalytic conditions, the CO release is faster than the bimolecular $1^{(II/I)}$-CO reduction from the reduced PS. Since the latter process depends on the catalyst and PS concentrations, under diluted conditions, it is expected that the reduction rate can be slow down, facilitating the CO release and the following intermediates of the photocatalytic cycle (green cycle, Scheme 4). An interesting connection between both catalytic cycles is the promotion of $1^{(I)}$ from

$1^{(I)}$-CO by light labilization of the M-CO bond in organometallic species. Indeed, light can be taken as an advantage to allow the electrocatalytic performance at $Co^{II/I}$ reduction potential. Another catalytic cycles interconnection is the potential formation of $Co(II)(CO)(CO_2H)$ (blue cycle, Scheme 4) from $Co(II)(CO_2H)$ + CO (green cycle, Scheme 4), which is slightly exergonic (-2.4 $kcal \cdot mol^{-1}$). However, further progress in this catalytic cycle is not viable under photocatalytic conditions due to the energetic uphill $Co^{(II/I)}(CO)(CO_2H)$ (-1.90 V) reduction, together with the less favorable C-O cleavage in $Co(II)(CO)(CO_2H)$ than in $Co(II)(CO2H)$. Therefore, at photochemical redox conditions, $Co(II)(CO)(CO_2H)$ can be assigned as an off-cycle resting state.

Finally, we would like to remark that a large number of potential interconnections between both catalytic cycles highlights the challenge and the need for an in-depth analysis, even in CO_2 reduction prototype reactions. To further progress into the understanding, more elaborated approaches should be taken, such as using graph theory to unravel all potential pathways and their weight into the global mechanism for given reaction conditions.

CONCLUSIONS

We have presented a detailed mechanistic investigation of electrochemical CO_2-to-CO reduction catalyzed by a new cobalt catalyst ($1^{(II)}$) based on a highly basic tetradentate aminopyridyl ligand. To the best of our knowledge, FTIR-SEC provides the first *in-situ* spectroscopic evidence for the formation of a Co^I-CO ($1^{(I)}$-CO, v_{CO} = 1910 cm^{-1}) resulting from the electrochemical CO_2-to-CO reduction at the non-catalytic $Co^{II/I}$ redox wave. This observation has relevant mechanistic implications since it shows that: 1) the electrochemically generated Co^I species ($1^{(I)}$) is nucleophilic enough to bind the CO_2 molecule and 2) the C-O bond cleavage can occur at room temperature, at mild applied potentials and with no added protons in acetonitrile. DFT modeling of the reaction mechanism has corroborated that both the CO_2 binding and the C-O bond cleavage steps are kinetically feasible at the $Co^{II/I}$ redox potential. However, the CO release from $1^{(I)}$-CO is a key limiting step which prevents the recovery of the catalytically active species $1^{(I)}$. Computational modeling of the different catalytic mechanisms in a broad potential and pH windows allowed for the rationalization of our experimental

observations. The catalytic mechanism is triggered by the one-electron reduction of $\mathbf{1^{(I)}}$-CO to the corresponding formal Co^0 which can only be afforded close to the Co$^{I/0}$ redox potential. Photocatalytic experiments under blue-light irradiation confirm the ability of $\mathbf{1^{(I)}}$ towards catalytic CO_2 reduction, even when the $E_{1/2}$ of the $\mathbf{PS_{Ir}}$ is not suitable for the $\mathbf{1^{(I/0)}}$-CO reduction. It is proposed that under photocatalytic conditions the CO release from $\mathbf{1^{(II)}}$-CO is kinetically favored over the $\mathbf{1^{(I)}}$-CO reduction due to the low concentration of catalyst and photosensitizers.

Finally, light-assisted electrocatalysis was successfully employed to improve the catalytic performance of $\mathbf{1^{(II)}}$ at -2.46 V reduction potential. The irradiation, favors the activation of inactive carbonyl species and reaching higher efficiency for CO production. In view of these findings, light-induced metal carbonyl dissociation was revealed as a promising strategy to mitigate CO catalyst poisoning. Finally, we have proposed a unified mechanistic view of the existing differences between photo- and electrochemical CO_2-to-CO reduction catalysis (Scheme 4). The results presented here will help to rationalize the behavior of other reported cobalt-based molecular electrocatalysts and to find out new approaches for the optimization of earth-abundant molecular catalysts.

ASSOCIATED CONTENT

Supporting Information

Methods of synthesis, characterization of reaction intermediates, catalytic studies and DFT studies. This material is available free of charge via the Internet at http://pubs.acs.org.

AUTHOR INFORMATION

Corresponding Author

E-mail: josepm.luis@udg.edu
E-mail: jlloret@iciq.es

Author Contributions

‡These authors contributed equally.

ACKNOWLEDGMENT

REFERENCES

(1) (a) Bushuyev, O. S.; De Luna, P.; Dinh, C. T.; Tao, L.; Saur, G.; van de Lagemaat, J.; Kelley, S. O.; Sargent, E. H. What Should We Make with CO_2 and How Can We Make It? *Joule* **2018**, *2*, 825; (b) De Luna, P.; Hahn, C.; Higgins, D.; Jaffer, S. A.; Jaramillo, T. F.; Sargent, E. H. What would it take for renewably powered electrosynthesis to displace petrochemical processes? *Science* **2019**, *364*, eaav3506.
(2) (a) Claros, M.; Ungeheuer, F.; Franco, F.; Martin-Diaconescu, V.; Casitas, A.; Lloret-Fillol, J. Reductive Cyclization of Unactivated Alkyl Chlorides with Tethered Alkenes under Visible-Light Photoredox Catalysis. *Angew. Chem. Int. Ed.* **2019**, *58*, 4869; (b) Lee, K. J.; Elgrishi, N.; Kandemir, B.; Dempsey, J. L. Electrochemical and spectroscopic methods for evaluating molecular electrocatalysts.

Nat. Rev. Chem. **2017**, *1*, 0039; (c) Grice, K. A. Carbon dioxide reduction with homogenous early transition metal complexes: Opportunities and challenges for developing CO_2 catalysis. *Coord. Chem. Rev.* **2017**, *336*, 78; (d) Bonin, J.; Maurin, A.; Robert, M. Molecular catalysis of the electrochemical and photochemical reduction of CO2 with Fe and Co metal based complexes. Recent advances. *Coord. Chem. Rev.* **2017**, *334*, 184.
(3) Fukuzumi, S.; Lee, Y.-M.; Ahn, H. S.; Nam, W. Mechanisms of catalytic reduction of CO_2 with heme and nonheme metal complexes. *Chem. Sci.* **2018**, *9*, 6017.
(4) Raymond, Z.; Jeannot, H.; Jean-Marie, L. Photogeneration of Carbon Monoxide and of Hydrogen via Simultaneous Photochemical Reduction of Carbon Dioxide and Water by Visible-Light Irradiation of Organic Solutions Containing Tris(2,2′-bipyridine)ruthenium(II) and Cobalt(II) Species as Homogeneous Catalysts. *Helv. Chim. Acta* **1986**, *69*, 1065.
(5) (a) Guo, Z.; Cheng, S.; Cometto, C.; Anxolabéhère-Mallart, E.; Ng, S.-M.; Ko, C.-C.; Liu, G.; Chen, L.; Robert, M.; Lau, T.-C. Highly Efficient and Selective Photocatalytic CO_2 Reduction by Iron and Cobalt Quaterpyridine Complexes. *J. Am. Chem. Soc.* **2016**, *138*, 9413; (b) Ouyang, T.; Huang, H.-H.; Wang, J.-W.; Zhong, D.-C.; Lu, T.-B. A Dinuclear Cobalt Cryptate as a Homogeneous Photocatalyst for Highly Selective and Efficient Visible-Light Driven CO_2 Reduction to CO in CH_3CN/H_2O Solution. *Angew. Chem.* **2017**, *129*, 756; (c) Jia-Wei, W.; Hai-Hua, H.; Jia-Kai, S.; Ting, O.; Di-Chang, Z.; Tong-Bu, L. Electrocatalytic and Photocatalytic Reduction of CO_2 to CO by Cobalt(II) Tripodal Complexes: Low Overpotentials, High Efficiency and Selectivity. *ChemSusChem* **2018**, *11*, 1025.
(6) (a) Chen, L.; Guo, Z.; Wei, X.-G.; Gallenkamp, C.; Bonin, J.; Anxolabéhère-Mallart, E.; Lau, K.-C.; Lau, T.-C.; Robert, M. Molecular Catalysis of the Electrochemical and Photochemical Reduction of CO_2 with Earth-Abundant Metal Complexes. Selective Production of CO vs HCOOH by Switching of the Metal Center. *J. Am. Chem. Soc.* **2015**, *137*, 10918; (b) Wang, F.; Cao, B.; To, W.-P.; Tse, C.-W.; Li, K.; Chang, X.-Y.; Zang, C.; Chan, S. L.-F.; Che, C.-M. The effects of chelating N_4 ligand coordination on Co(II)-catalysed photochemical conversion of CO_2 to CO: reaction mechanism and DFT calculations. *Catalysis Science & Technology* **2016**, *6*, 7408; (c) Chan, S. L.-F.; Lam, T. L.; Yang, C.; Yan, S.-C.; Cheng, N. M. A robust and efficient cobalt molecular catalyst for CO_2 reduction. *Chem. Commun.* **2015**, *51*, 7799.
(7) (a) Francke, R.; Schille, B.; Roemelt, M. Homogeneously Catalyzed Electroreduction of Carbon Dioxide—Methods, Mechanisms, and Catalysts. *Chem. Rev.* **2018**; (b) Elgrishi, N.; Chambers, M. B.; Wang, X.; Fontecave, M. Molecular polypyridine-based metal complexes as catalysts for the reduction of CO_2. *Chem. Soc. Rev.* **2017**, *46*, 761; (c) Takeda, H.; Cometto, C.; Ishitani, O.; Robert, M. Electrons, Photons, Protons and Earth-Abundant Metal Complexes for Molecular Catalysis of CO_2 Reduction. *ACS Cat.* **2017**, *7*, 70.
(8) (a) Cometto, C.; Chen, L.; Lo, P.-K.; Guo, Z.; Lau, K.-C.; Anxolabéhère-Mallart, E.; Fave, C.; Lau, T.-C.; Robert, M. Highly Selective Molecular Catalysts for the CO_2-to-CO Electrochemical Conversion at Very Low Overpotential. Contrasting Fe vs Co Quaterpyridine Complexes upon Mechanistic Studies. *ACS Cat.* **2018**, *8*, 3411; (b) Chapovetsky, A.; Welborn, M.; Luna, J. M.; Haiges, R.; Miller, T. F.; Marinescu, S. C. Pendant Hydrogen-Bond Donors in Cobalt Catalysts Independently Enhance CO_2 Reduction. *ACS Cent. Sci.* **2018**, *4*, 397.
(9) (a) Che, C.-M.; Mak, S.-T.; Lee, W.-O.; Fung, K.-W.; Mak, T. C. W. Electrochemical studies of nickel(II) and cobalt(II) complexes of tetra-azamacrocycles bearing a pyridine functional group and X-ray structures of [Ni(L$_3$)Cl]ClO$_4$ and [Ni(L$_3$)][ClO$_4$]$_2$·H$_2$O {L$_3$=meso-2,3,7,11,12-pentamethyl-3,7,11,17-tetra-azabicyclo[11.3.1]heptadeca-1(17),13,15-triene}. *J. Chem. Soc., Dalton Trans.* **1988**, 2153; (b) Elgrishi, N.; Chambers, M. B.; Fontecave, M. Turning it off! Disfavouring hydrogen evolution to enhance selectivity for CO production during homogeneous CO_2 reduction by cobalt-terpyridine complexes. *Chem. Sci.* **2015**, *6*, 2522; (c) Shimoda, T.; Morishima, T.; Kodama, K.; Hirose, T.; Polyansky, D. E.; Manbeck, G. F.; Muckerman, J. T.; Fujita, E. Photocatalytic CO_2 Reduction by Trigonal-Bipyramidal Cobalt(II) Polypyridyl Complexes: The Nature of Cobalt(I) and Cobalt(0) Complexes upon Their Reactions with CO_2, CO, or Proton. *Inorg. Chem.* **2018**.

(10) Fukatsu, A.; Kondo, M.; Okabe, Y.; Masaoka, S. Electrochemical analysis of iron-porphyrin-catalyzed CO_2 reduction under photoirradiation. *J. Photoch. Photobio. A.* **2015**, *313*, 143.

(11) Steinlechner, C.; Roesel, A. F.; Oberem, E.; Päpcke, A.; Rockstroh, N.; Gloaguen, F.; Lochbrunner, S.; Ludwig, R.; Spannenberg, A.; Junge, H.; Francke, R.; Beller, M. Selective Earth-Abundant System for CO_2 Reduction: Comparing Photo- and Electrocatalytic Processes. *ACS Cat.* **2019**, *9*, 2091.

(12) (a) Fujita, E.; Furenlid, L. R.; Renner, M. W. Direct XANES Evidence for Charge Transfer in Co−CO_2 Complexes. *J. Am. Chem. Soc.* **1997**, *119*, 4549; (b) Fujita, E.; van Eldik, R. Effect of Pressure on the Reversible Binding of Acetonitrile to the "Co(I)−CO_2" Adduct To Form Cobalt(III) Carboxylate. *Inorg. Chem.* **1998**, *37*, 360; (c) Ogata, T.; Yanagida, S.; Brunschwig, B. S.; Fujita, E. Mechanistic and Kinetic Studies of Cobalt Macrocycles in a Photochemical CO_2 Reduction System: Evidence of Co-CO_2 Adducts as Intermediates. *J. Am. Chem. Soc.* **1995**, *117*, 6708; (d) Fujita, E.; Creutz, C.; Sutin, N.; Szalda, D. J. Carbon dioxide activation by cobalt(I) macrocycles: factors affecting carbon dioxide and carbon monoxide binding. *J. Am. Chem. Soc.* **1991**, *113*, 343; (e) Fujita, E.; Szalda, D. J.; Creutz, C.; Sutin, N. Carbon dioxide activation: thermodynamics of carbon dioxide binding and the involvement of two cobalt centers in the reduction of carbon dioxide by a cobalt(I) macrocycle. *J. Am. Chem. Soc.* **1988**, *110*, 4870.

(13) (a) Gangi, D. A.; Durand, R. R. Binding of carbon dioxide to cobalt and nickel tetra-aza macrocycles. *J. Chem. Soc., Chem. Commun.* **1986**, 697; (b) Schmidt, M. H.; Miskelly, G. M.; Lewis, N. S. Effects of redox potential, steric configuration, solvent, and alkali metal cations on the binding of carbon dioxide to cobalt(I) and nickel(I) macrocycles. *J. Am. Chem. Soc.* **1990**, *112*, 3420; (c) Schneider, J.; Jia, H.; Muckerman, J. T.; Fujita, E. Thermodynamics and kinetics of CO_2, CO, and H+ binding to the metal centre of CO_2 reductioncatalysts. *Chem. Soc. Rev.* **2012**, *41*, 2036.

(14) Lacy, D. C.; McCrory, C. C. L.; Peters, J. C. Studies of Cobalt-Mediated Electrocatalytic CO_2 Reduction Using a Redox-Active Ligand. *Inorg. Chem.* **2014**, *53*, 4980.

(15) Fisher, B. J.; Eisenberg, R. Electrocatalytic reduction of carbon dioxide by using macrocycles of nickel and cobalt. *J. Am. Chem. Soc.* **1980**, *102*, 7361.

(16) (a) Froehlich, J. D.; Kubiak, C. P. The Homogeneous Reduction of CO_2 by [Ni(cyclam)]+: Increased Catalytic Rates with the Addition of a CO Scavenger. *J. Am. Chem. Soc.* **2015**, *137*, 3565; (b) Lieske, L. E.; Rheingold, A.; Machan, C. W. Electrochemical reduction of carbon dioxide with a molecular polypyridyl nickel complex. *Sustainable Energy Fuels* **2018**, *2*, 1269

(17) Shimoda, T.; Morishima, T.; Kodama, K.; Hirose, T.; Polyansky, D. E.; Manbeck, G. F.; Muckerman, J. T.; Fujita, E. Photocatalytic CO_2 Reduction by Trigonal-Bipyramidal Cobalt(II) Polypyridyl Complexes: The Nature of Cobalt(I) and Cobalt(0) Complexes upon Their Reactions with CO_2, CO, or Proton. *Inorg. Chem.* **2018**, *57*, 5486.

(18) Call, A.; Franco, F.; Kandoth, N.; Fernandez, S.; Gonzalez-Bejar, M.; Perez-Prieto, J.; Luis, J. M.; Lloret-Fillol, J. Understanding light-driven H2 evolution through the electronic tuning of aminopyridine cobalt complexes. *Chem. Sci.* **2018**, *9*, 2609.

(19) (a) Call, A.; Casadevall, C.; Acuña-Parés, F.; Casitas, A.; Lloret-Fillol, J. Dual cobalt–copper light-driven catalytic reduction of aldehydes and aromatic ketones in aqueous media. *Chem. Sci.* **2017**, *8*, 4739; (b) Call, A.; Lloret-Fillol, J. Enhancement and control of the selectivity in light-driven ketone versus water reduction using aminopyridine cobalt complexes. *Chem. Commun.* **2018**, *54*, 9643.

(20) (a) Franco, F.; Cometto, C.; Nencini, L.; Barolo, C.; Sordello, F.; Minero, C.; Fiedler, J.; Robert, M.; Gobetto, R.; Nervi, C. Local Proton Source in Electrocatalytic CO_2 Reduction with [Mn(bpy–R)(CO)3Br] Complexes. *Chem. Eur. J.* **2017**, *23*, 4782; (b) Franco, F.; Pinto, M. F.; Royo, B.; Lloret-Fillol, J. A Highly Active N-Heterocyclic Carbene Manganese(I) Complex for Selective Electrocatalytic CO_2 Reduction to CO. *Angew. Chem. Int. Ed.* **2018**, *57*, 4603.

(21) Krejčik, M.; Daněk, M.; Hartl, F. Simple construction of an infrared optically transparent thin-layer electrochemical cell: Applications to the redox reactions of ferrocene, $Mn_2(CO)_{10}$ and Mn(CO)3(3,5-di-t-butyl-catecholate)−. *J. Electroanal. Chem.* **1991**, *317*, 179.

(22) (a) Szalda, D. J.; Fujita, E.; Creutz, C. Cobalt(I), -(II), and -(III) complexes of a tetraaza 14-membered macrocycle, 5,7,7,12,14,14-hexamethyl-1,4,8,11-tetraazacyclotetradeca-4,11-diene (L). Crystal and molecular structures of [CoL(CO)]ClO4, trans-CoLCl2, and cis-[CoL(CO3)]ClO4. *Inorg. Chem.* **1989**, *28*, 1446; (b) Shaffer, D. W.; Johnson, S. I.; Rheingold, A. L.; Ziller, J. W.; Goddard, W. A.; Nielsen, R. J.; Yang, J. Y. Reactivity of a Series of Isostructural Cobalt Pincer Complexes with CO_2, CO, and H+. *Inorg. Chem.* **2014**, *53*, 13031; (c) Fujita, E.; Creutz, C.; Sutin, N.; Brunschwig, B. S. Carbon dioxide activation by cobalt macrocycles: evidence of hydrogen bonding between bound CO_2 and the macrocycle in solution. *Inorg. Chem.* **1993**, *32*, 2657.

(23) Planas, O.; Whiteoak, C. J.; Martin-Diaconescu, V.; Gamba, I.; Luis, J. M.; Parella, T.; Company, A.; Ribas, X. Isolation of Key Organometallic Aryl-Co(III) Intermediates in Cobalt-Catalyzed C(sp2)–H Functionalizations and New Insights into Alkyne Annulation Reaction Mechanisms. *J. Am. Chem. Soc.* **2016**, *138*, 14388.

(24) Planas, O.; Roldán-Gómez, S.; Martin-Diaconescu, V.; Luis, J. M.; Company, A.; Ribas, X. Mechanistic insights into the S_N2-type reactivity of aryl-Co(III) masked-carbenes for C–C bond forming transformations. *Chem. Sci.* **2018**, *9*, 5736.

(25) King, A. E.; Surendranath, Y.; Piro, N. A.; Bigi, J. P.; Long, J. R.; Chang, C. J. A mechanistic study of proton reduction catalyzed by a pentapyridine cobalt complex: evidence for involvement of an anation-based pathway. *Chem. Sci.* **2013**, *4*, 1578.

(26) (a) Tokmic, K.; Markus, C. R.; Zhu, L.; Fout, A. R. Well-Defined Cobalt(I) Dihydrogen Catalyst: Experimental Evidence for a Co(I)/Co(III) Redox Process in Olefin Hydrogenation. *J. Am. Chem. Soc.* **2016**, *138*, 11907; (b) Marlier, E. E.; Ulrich, B. A.; McNeill, K. Synthesis and Reactivity of an Isolable Cobalt(I) Complex Containing a β-Diketiminate-Based Acyclic Tetradentate Ligand. *Inorg. Chem.* **2012**, *51*, 2079.

(27) *In order to better model the CO concentration at the beggining of the reaction it has been set to 50 μM. If considering a CO concentration to be 1 mM, the energy correction due to concentration change was 1.8 kcal·mol^{-1}.*

(28) Fujita, E. Photochemical carbon dioxide reduction with metal complexes. *Coord. Chem. Rev.* **1999**, *185-186*, 373.

(29) Dey, S.; Ahmed, M. E.; Dey, A. Activation of Co(I) State in a Cobalt-Dithiolato Catalyst for Selective and Efficient CO2 Reduction to CO. *Inorg. Chem.* **2018**, *57*, 5939.

(30) Kozuch, S.; Shaik, S. How to Conceptualize Catalytic Cycles? The Energetic Span Model. *Acc. Chem. Res.* **2011**, *44*, 101.

(31) Medford, A. J.; Shi, C.; Hoffmann, M. J.; Lausche, A. C.; Fitzgibbon, S. R.; Bligaard, T.; Nørskov, J. K. CatMAP: A Software Package for Descriptor-Based Microkinetic Mapping of Catalytic Trends. *Catal. Lett.* **2015**, *145*, 794.

(32) (a) Wrighton M. Photochemistry of metal carbonyls *Chem. Rev.* **1974**, *74*, 401; (b) Geoggroy, G. L.; Wrighton, M. S. *2 Metal Carbonyls. Organometallic Photochemistry*, 1st Edition, Academic Press: London, 1979, pp 34-162; (c) Mirbach, M. F.; Wegman, R. W. Photochemical ligand dissociation, electron transfer, and metal-metal bond cleavage of phosphine-substituted cobalt carbonyl complexes, *Organometallics* **1984**, *3*, 900.

Insert Table of Contents artwork here